

Large scale structure and dark energy

Ph.D Thesis in Physics
Universitat de Barcelona
Departament d'Astronomia i Meteorologia

(Programa de doctorat bienni 2003-2005)

Anna Cabré Albós
Supervisor: Enrique Gaztañaga Balbás

Tutor: Eduard Salvador Solé

Barcelona 2008

Part I

Structure formation through cross-correlating sky maps

Chapter 2

The Integrated Sachs-Wolfe effect

In this chapter we present the Integrated Sachs-Wolfe effect and how we can detect it through the cross-correlation of CMB temperature fluctuations with number density fluctuations in large scale structure. We explain also the prediction in configuration space obtained from harmonic space prediction.

2.1 Integrated Sachs-Wolfe effect introduction

The temperature of CMB photons can be influenced by any field which couples to photons. The dominant effects of these fields occur at the surface of last scattering, but there are also secondary effects in the way of the photons from CMB to us. The Integrated Sachs-Wolfe effect (ISW) is a net gravitational blue shifting (or red shifting) when photons from CMB fall into a deep potential valley gaining some energy (blueshift) and climb back out of a shallow potential (redshift). Or the reverse way. This effect happens when there is an evolving gravitational potential, either because the universe is flat or because there is a component of dark energy. In a flat universe Λ CDM, the late ISW effect tells us about the time that matter ceases to dominate (early ISW happens around the time radiation ceases to dominate). These secondary temperature anisotropies are therefore correlated with local, evolving, structures on large scales. For a universe without dark energy (Einstein-de-Sitter cosmology) there is no cross-correlation signal because the gravitational potential remains constant, despite the linear growth of matter fluctuations. The correlation is negative when the structures grow faster than in the Einstein-de-Sitter cosmology, because the increasing potential redshifts photons and leaves a cold spot in the CMB sky. Otherwise the correlation is positive. The ISW effect is expected to produce an increase of power (a bump) in the amplitude of the CMB fluctuations at the largest scales, ie lower order multipoles, which are dominated by cosmic variance. At small scales photons pass through so many potentials wells that there is an almost net cancellation in the gravitational redshift. This expectation, seems challenged by observations, as the first year WMAP results (WMAP1) confirmed the low amplitude of the CMB quadrupole first measured by COBE (Hinshaw et al. 2003). The discrepancy between the observations and the Λ CDM model is particularly evident in the temperature angular correlation function $w_2(\theta)$, which shows an almost complete lack of signal on angular scales $\theta \gtrsim 60$ degrees. According to Spergel et al. (2007), the probability of finding such a result in a spatially-flat Λ CDM cosmology is about 1.5×10^{-3} . This was questioned in Gaztañaga et al. (2003) who found, using simulated Λ CDM WMAP maps, a much lower significance (less than 2-sigma) for $w_2(\theta)$. A low significance was also estimated by different studies (eg Efstathiou 2003, de Oliveira-Costa et al. 2004), although a discrepancy larger than 3-sigma still remains

on both the quadrupole-octopole alignment (Tegmark et al. 2003, de Oliveira-Costa et al. 2004) and the WMAP observed high value of the temperature-polarization cross-correlation on large scales (Doré et al. 2004).

Given the observed anomalies on the ISW predictions, it is of particular interest to check if the ISW effect can be detected observationally through an independent test, such as the cross-correlation of temperature fluctuations with local tracers of the gravitational potential (Crittenden & Turok 1996). A positive cross-correlation between WMAP1 and galaxy samples from the Sloan Digital Sky Survey (SDSS) was first found by Fosalba et al. (2003) (FGC03 from now on) and Scranton et al. (2003). FGC03 used the 1yr WMAP data (WMAP1) and the SDSS data release 1 (SDSS1). WMAP1 has also been correlated with the APM galaxies (Fosalba & Gaztañaga 2004), infrared galaxies (Afshordi et al. 2004), radio galaxies (Nolta et al. 2004), the hard X-ray background (Boughn & Crittenden 2004a,b) and luminous red galaxies (Padmanabhan et al. 2005). The significance of these cross-correlations measurements was low (about 2-3 σ , see Gaztañaga et al. (2006) for a summary and joint analysis), and many scientists are still skeptical of the reality of these detections. A higher significance is found in Chapter 6 when cross-correlating WMAP3 with SDSS data release 4. Giannantonio et al. 2006 has correlated WMAP3 with a photometric selection of SDSS quasars and have done a new compilation with the new detections, where one can see that the best fit WMAP Λ CDM flat model is consistent with data from ISW effect, but with a tendency to higher Ω_Λ values, which has to be well understood. The WMAP3 temperature fluctuations has also been correlated with 2MASS by Rassat et al. (2007) Giannantonio et al. (2008) have done a combined analysis of the Integrated Sachs-Wolfe effect after this work was done.

2.2 Cross-correlation in configuration space from harmonic space

One way to detect the ISW effect is to cross-correlate temperature fluctuations with galaxy density fluctuations projected on the sky (Crittenden & Turok 1996). When photons coming from last scattering surface CMB pass through gravitational potentials created by large scale structure, they modify the temperature through the following equation, given by ISW temperature anisotropies (Sachs & Wolfe 1967):

$$\Delta_T^{ISW}(\hat{n}) \equiv \frac{T(\hat{n}) - T_0}{T_0} = - \int dz \frac{d}{dz} (\Phi - \Psi) = -2 \int dz \frac{d\Phi}{dz}(\hat{n}, z) \quad (2.1)$$

where Φ and Ψ are the Newtonian gravitational potentials ($\Phi = -\Psi$ for non anisotropic stress) and we suppose an instantaneous reionization with $\tau = \infty$ before the reionization redshift and $\tau = 0$ after that.

We want to calculate the cross-correlation $w_{TG}^{ISW}(\theta) = \langle \Delta_T^{ISW}(\hat{n}_1) \delta_G(\hat{n}_2) \rangle$ of CMB temperature with large scale structure, which is useful to expand in a Legendre polynomial basis. On large linear scales and small angular separations it is:

$$w_{TG}^{ISW}(\theta) = \sum_{\ell} \frac{2\ell + 1}{4\pi} p_{\ell}(\cos \theta) C_{GT}^{ISW}(\ell) \quad (2.2)$$

Let's suppose that we have two fields $A(\vec{x})$ and $B(\vec{x})$ in 3D which we want to project on the sky to calculate the correlation between them. We define their Fourier transforms as

$$A(\vec{k}) = \int d^3\vec{x} e^{-i\vec{k}\cdot\vec{x}} A(\vec{x}), \quad B(\vec{k}) = \int d^3\vec{x} e^{-i\vec{k}\cdot\vec{x}} B(\vec{x}). \quad (2.3)$$

The cross-correlation power spectrum, $P_{AB}(k)$ is defined by

$$\langle A_{\vec{k}_1} B_{\vec{k}_2} \rangle = (2\pi)^3 \delta^3(\vec{k}_1 - \vec{k}_2) P_{AB}(k_1). \quad (2.4)$$

The projections of A and B on the sky are defined using F_A and F_B projection kernels

$$\tilde{A}(\hat{n}) = \int dr F_A(r) A(r\hat{n}), \quad \text{and} \quad \tilde{B}(\hat{n}) = \int dr F_B(r) B(r\hat{n}). \quad (2.5)$$

For the projected galaxy overdensity, this kernel is

$$F_g(r) = \frac{r^2 \phi(r)}{\int dr' r'^2 \phi(r')}. \quad (2.6)$$

where $\phi(r)$ is the survey galaxy selection function and $r(z)$ is the comoving distance.

Now, expanding \tilde{A} and \tilde{B} in terms of spherical harmonics, the cross-power spectrum, $C_{AB}(\ell)$ is defined as

$$\begin{aligned} C_{AB}(\ell) &\equiv \langle \tilde{A}_{\ell m} \tilde{B}_{\ell m}^* \rangle \\ &= \int dr_1 dr_2 F_A(r_1) F_B(r_2) \times \\ &\int \frac{d^3 \vec{k}}{(2\pi)^3} P_{AB}(k) (4\pi)^2 j_\ell(kr_1) j_\ell(kr_2) Y_{\ell m}(\hat{k}) Y_{\ell m}^*(\hat{k}) \\ &= \int dr_1 dr_2 F_A(r_1) F_B(r_2) \int \frac{2k^2 dk}{\pi} j_\ell(kr_1) j_\ell(kr_2) P_{AB}(k), \end{aligned} \quad (2.7)$$

where j_ℓ 's are the spherical Bessel functions of rank ℓ and $Y_{\ell m}$'s are the spherical harmonics. We have used the Rayleigh expansion for a plane wave with Bessel functions,

$$e^{i\vec{k} \cdot \vec{x}} = 4\pi \sum_{\ell, m} i^\ell j_\ell(kr) Y_{\ell m}^*(\hat{k}) Y_{\ell m}(\hat{n}) \quad (2.8)$$

and also Eq.(2.3), Eq.(2.4) and Eq.(2.5). To proceed further, we use the small angle (large ℓ) approximation for the spherical Bessel functions

$$j_\ell(x) = \sqrt{\frac{\pi}{2\ell + 1}} [\delta_{\text{Dirac}}(\ell + \frac{1}{2} - x) + \mathcal{O}(\ell^{-2})], \quad (2.9)$$

which yields

$$C_{AB}(\ell) = \int \frac{dr}{r^2} F_A(r) F_B(r) P_{AB} \left(\frac{\ell + 1/2}{r} \right) \cdot [1 + \mathcal{O}(\ell^{-2})]. \quad (2.10)$$

This is the so called Limber equation, with an error that decreases as ℓ^{-2} , inaccurate for small multipoles. However, the sum in Eq.(12.3) begins from $\ell = 2$ because the monopole ($\ell = 0$) and dipole ($\ell = 1$) have been removed from WMAP temperature fluctuations map, so we can consider this one a good approximation.

We can relate the power spectrum of the cross-correlation to the auto-power spectrum $P(k)$

$$\langle \delta_k \delta_{k'} \rangle = (2\pi)^3 \delta^D(\vec{k} - \vec{k}') P(k) \quad (2.11)$$

using the Poisson equation for the gravitational potential in temperature fluctuations,

$$\Delta^2 \phi = 4\pi G a^2 \delta\rho(\mathbf{x}) \quad (2.12)$$

and his Fourier transform

$$\phi(k) = -\frac{4\pi G}{a} \frac{\rho_m}{k^2} \delta(k, z) = -\frac{3}{2} \frac{\Omega_M}{a} \frac{H_0^2}{k^2} \delta(k, z) \quad (2.13)$$

For the overdensity in large scale structure fluctuations, we assume a constant galaxy bias, b_g , which relates the galaxy fluctuations, δ_g , to the overall matter density fluctuations δ_m

$$\delta_g = b_g \delta_m \quad (2.14)$$

and we arrive to the following equations

$$\begin{aligned} C_{GT}^{ISW}(\ell) &= \frac{4}{(2\ell + 1)^2} \int dz W_{ISW}(z) W_G(z) \frac{H(z)}{c} P(k) \\ W_{ISW}(z) &= 3\Omega_m (H_0/c)^2 \frac{d[D(z)/a]}{dz} \\ W_G(z) &= b(z) \phi_G(z) D(z), \end{aligned} \quad (2.15)$$

where $k = \frac{\ell+1/2}{r}$, $\phi_G(z)$ is the survey galaxy selection function, $r(z)$ is the comoving distance, $b(z)$ is the galaxy bias at a redshift z , $D(z)$ the lineal growth function which relates the overdensity at a redshift z to the one at redshift 0, normalized to unity at present, $\delta(k, z) = D(z)\delta(k, 0)$. The Hubble equation: $H(z)^2/H_0^2 = \Omega_M(1+z)^3 + \Omega_\Lambda(1+z)^{3(1+w)}$ relates the comoving distance with the redshift (in our case we consider a flat universe and dark energy models with an effective equation of state $w = p/\rho$). This is just a Legendre decomposition of the equations presented in Fosalba & Gaztañaga (2004), see also Afshordi (2004). The advantage of this formulation is that we can here set the monopole ($\ell = 0$) and dipole ($\ell = 1$) contribution to zero, as it is done in the WMAP maps. The contribution of the monopole and dipole to w_{TG} is significant and over predicts w_{TG} by about 10%. The power spectrum is $P(k) = A k^{n_s} T^2(k)$, where $T(k)$ is the Λ CDM transfer function, which we evaluate using the fitting formula of Eisenstein & Hu (1998).

2.3 How to obtain cross-correlation in real data

We define the cross-correlation function as the expectation value of density fluctuations $\delta_G = N_G / \langle N_G \rangle - 1$ and temperature anisotropies $\Delta_T = T - T_0$ (in μK) at two angular positions \hat{n}_1 and \hat{n}_2 in the sky: $w_{TG}(\theta) \equiv \langle \Delta_T(\hat{n}_1) \delta_G(\hat{n}_2) \rangle$, where $\theta = |\hat{n}_2 - \hat{n}_1|$, assuming that the distribution is statistically isotropic. To estimate $w_{TG}(\theta)$ from the pixel maps we use:

$$w_{TG}(\theta) = \frac{\sum_{i,j} \Delta_T(\hat{n}_i) \delta_G(\hat{n}_j) w_i w_j}{\sum_{i,j} w_i w_j}, \quad (2.16)$$

where the sum extends to all pairs i, j separated by $\theta \pm \Delta\theta$. The weights w_i can be used to minimize the variance when the pixel noise is not uniform, however this introduces larger cosmic variance. Here we follow the WMAP team and use uniform weights (i.e. $w_i = 1$).

Chapter 3

Errors analysis in the cross-correlation

Constraining cosmological parameters from measurements of the Integrated Sachs-Wolfe effect requires developing robust and accurate methods for computing statistical errors in the cross-correlation between maps. This chapter presents a detailed comparison of such error estimation applied to the case of cross-correlation of Cosmic Microwave Background (CMB) and large-scale structure data. We compare theoretical models for error estimation with Monte Carlo simulations where both the galaxy and the CMB maps vary around a fiducial auto-correlation and cross-correlation model which agrees well with the current concordance Λ CDM cosmology. Our analysis compares estimators both in harmonic and configuration (or real) space, quantifies the accuracy of the error analysis and discuss the impact of partial sky survey area and the choice of input fiducial model on dark-energy constraints. We show that purely analytic approaches yield accurate errors even in surveys that cover only 10% of the sky and that parameter constraints strongly depend on the fiducial model employed. Alternatively, we discuss the advantages and limitations of error estimators that can be directly applied to data. In particular, we show that errors and covariances from the jackknife method agree well with the theoretical approaches and simulations. We also introduce a novel method in real space that is computationally efficient and can be applied to real data and realistic survey geometries. Finally, we present a number of new findings and prescriptions that can be useful for analysis of real data and forecasts, and present a critical summary of the analyses done to date. This work can be found in Cabré et al. (2007).

3.1 Introduction to errors and literature

Sample variance from the primary CMB anisotropies limits the ability with which one can detect CMB-LSS correlations. For the observationally favored flat Λ CDM model, even an optimal measurement of the cross-correlation could only achieve a signal-to-noise ratio of ~ 10 (Crittenden & Turok 1996; Peiris & Spergel 2000; Afshordi 2004). Given the low significance level of ISW detections, a good understanding of the systematic and statistical errors is crucial to optimally exploit CMB-LSS correlation data that will be collected in future surveys such as PLANCK, DES, SPT, LSST, etc., for cosmological purposes (see e.g., Pogosian et al. 2005). Recent work has focused on the impact of known systematics on cross-correlation measurements (Boughn & Crittenden 2004a; Afshordi et al. 2004), however no detailed analysis has been carried out to assess how different error estimates compare or what is the accuracy delivered by each of them. So far, most of the published analyses have implemented one specific

error estimator (primarily in real or configuration space) without justifying the choice of that particular estimator or quantifying its degree of accuracy.

In particular, most of the groups that first claimed ISW detections (Boughn & Crittenden 2004a; Nolta et al. 2004; Fosalba & Gaztañaga 2004; Fosalba et al. 2003; Scranton et al. 2003; Rassat et al. 2007) estimated errors from CMB Gaussian Monte Carlo (MC) simulations alone. In this approach statistical errors are obtained from the dispersion of the cross-correlation between the CMB sky realizations with a (single) fixed observed map tracing the nearby large-scale structure. This estimator is expected to be reasonably accurate as long as the cross-correlation signal is weak and the CMB auto-correlation dominates the total variance of the estimator. We shall call this error estimator MC1 (see below).

Fosalba et al. (2003); Fosalba & Gaztañaga (2004) also used jackknife (JK) errors. They found that the JK errors perform well as compared to the MC1 estimator, but the JK error from the real data seems up to a factor of two smaller (on sub-degree scales) than the JK error estimated from simulations. This discrepancy arise from the fact that the fiducial theoretical model used in the MC1 simulations does not match the best fit to the data (see conclusions).

Afshordi et al. (2004) criticize the MC1 and JK estimators and implement a purely theoretical Gaussian estimator in harmonic space (which we shall call TH bellow). However, they did not show why their choice of estimator should be more optimal or validate it with simulations. This criticism to the JK approach has been spread in the literature without any critical assessment. Vielva et al. (2006) also point out the apparent limitations of the JK method and adopted the MC1 simulations instead. However they seem to find that the signal-to-noise of their measurement depends on the statistical method used.

Padmanabhan et al. (2005) use Fisher matrix approach and MC1-type simulations to validate and calibrate their errors. They also claim that JK errors tend to underestimate errors because of the small number of uncorrelated JK patches on the sky, but they provide no proof of that.

Giannantonio et al. (2006) use errors from MC simulations that follow the method put forward by Boughn et al. (1998). In their work the error estimator is built from pairs of simulation maps (of the CMB and large-scale structure fields) including the predicted auto and cross-correlation. This is the estimator we shall name MC2 below. They point out that their results are consistent with what is obtained from the simpler MC1 estimator. See also Giannantonio et al. (2008) for a recent study of MC1, MC2 and also JK errors.

In this part we develop a systematic approach to compare different error estimators in cross-correlation analyses. Armed with this machinery, we address some of the open questions that have been raised in previous work on the ISW effect detection: how accurate are JK errors? Are error estimators different due to the input theoretical models or the data themselves? How many Monte Carlo simulations should one use to get accurate results? Can we safely neglect the cross-correlation signal in the simulations? Do harmonic and real space methods yield compatible results? What is the uncertainty associated to the different error estimates?

The methodology and results presented here should apply to other cross-correlation analyses of different sky maps such as galaxy-galaxy or lensing-galaxy studies.

Table 3.1: Notation used in this part.

TC	Theory in Configuration space
TH	Theory in Harmonic space
MC	Monte Carlo simulations
MC2	MC of the 2 fields, with correlation signal
MC1	MC of 1 field alone (CMB), no correlation signal
JK	Jackknife errors
MC2-w	errors in w_{TG} from MC2 simulations
MC1-w	errors in w_{TG} from MC1 simulations
MC2- C_ℓ	errors in C_ℓ from MC2 simulations
TH-w	errors in w_{TG} from TH theory
TC-w	errors in w_{TG} from TC theory
TH- C_ℓ	errors in C_ℓ from TH theory
JK-w	errors in w_{TG} from JK simulations

3.2 Introduction to the methods to calculate errors

We consider four methods to estimate errors. The first one is based on Monte Carlo (MC) simulations of the pair of maps we want to correlate. We consider two variants: MC2, where pairs are correlated with a given fiducial model and MC1, where one map in each pair is fixed and no cross-correlation signal is included. The next two methods rely on theoretical estimation. We will use a popular harmonic space prediction, that we shall call TH (Theory in Harmonic space). We will also compare all these errors with a novel error estimator that is an analytic function of the auto and cross-correlation of the fields in real space that we shall call TC (Theory in Configuration space), an approach done by Marc Manera. Finally, we will estimate jackknife (JK) errors which uses sub-regions of the actual data map to calculate the dispersion in our estimator.

Once we have errors estimated in one space, it is also possible to translate them, through Legendre transformation, into the complementary space. We shall make a clear distinction between the method for the error calculation (i.e., MC, TH, TC or JK), and the estimator onto which the errors are propagated: i.e. either $w(\theta)$ or C_ℓ . For example, $TH - w$ means errors in $w(\theta)$ propagated from theoretical errors originally computed in harmonic space. This notation is summarized in Table 3.1.

In all cases (except for the JK) we are assuming Gaussian statistics. In principle, it is also possible to do all this with non-Gaussian statistics but this requires particular non-Gaussian models, which are currently not well motivated by observations. Ultimately, our focus here is on the comparison of different methods for a well defined set of reasonable assumptions.

3.3 Monte Carlo simulations (MC)

Pablo Fosalba has run 1000 Monte Carlo (MC) simulation pairs of the CMB temperature anisotropy and the dark-matter over-density field, including its cross-correlation, following the approach presented in Boughn et al. (1998) (see Eq.(3.2) below). These simulations are

produced using the *synfast* routine of the Healpix package¹. We assume that both fields are Gaussian: this is a good approximation for the CMB field on the largest scales (i.e few degrees on the sky), which are the relevant scales for the ISW effect. However, the matter density field is weakly non-linear on these scales (eg see Bernardeau et al. 2002) and therefore non-Gaussian, i.e it has non-vanishing higher-order moments. Therefore our simulations are realistic as long as non-Gaussianity does not significantly alter the CMB-matter cross-correlation and its associated errors.² We take galaxies to be fair tracers of the underlying spatial distribution of the matter density field on large-scales: we assume that a simple linear bias model relates both fields, so that $w_{GG} = b^2 w_{MM}$ and $w_{TG} = b w_{TM}$. Therefore, in what follows, we make no difference between matter and galaxies in our analysis (other than b), without loss of generality.

Decomposing our simulated fields on the sphere, we have

$$f(\hat{n}) = \sum_{\ell m} a_{\ell m} Y_{\ell m}(\hat{n}) \quad (3.1)$$

where $a_{\ell m}$ are the amplitudes of the scalar field projected on the spherical harmonic basis $Y_{\ell m}$. In our simulations, the $a_{\ell m}$'s are given by linear combinations of unit variance random Gaussian fields ψ ,

$$\begin{aligned} a_{\ell m}^T &= \sqrt{C_\ell^{TT}} \psi_{1,\ell m}, \\ a_{\ell m}^G &= \frac{C_\ell^{TG}}{\sqrt{C_\ell^{TT}}} \psi_{1,\ell m} + \left(C_\ell^{GG} - \frac{[C_\ell^{TG}]^2}{C_\ell^{TT}} \right)^{1/2} \psi_{2,\ell m} \end{aligned} \quad (3.2)$$

for the CMB temperature (T) and galaxy over-density (G) fields, respectively, and C_ℓ^{XY} is the (cross) angular power spectrum of the X and Y fields.

Our simulations assume a model that is broadly speaking in agreement with current observations, although the precise choice of parameter values is not critical for the purpose of this paper. We assume adiabatic initial conditions and a spatially flat FRW model with the following fiducial cosmological parameters: $\Omega_{DE} = 0.7$, $\Omega_B = 0.05$, $\Omega_\nu = 0$, $n = 1$, $h = 0.7$, $\sigma_8 = 0.9$. Although we will base most of our analyses on this fiducial model, we have also run a set of 1000 MC simulations for a more strongly dark-energy dominated Λ CDM model with $\Omega_{DE} = 0.8$ (other parameters remain as in our fiducial model). This will allow us to test how robust are our main results to changes around our fiducial model.

Galaxies are distributed in redshift according to an analytic selection function,

$$\frac{dN}{dz} = \frac{3}{2} \frac{z^2}{z_0^3} e^{-(z/z_0)^{3/2}} \quad (3.3)$$

where $z_m = 1.412 z_0$ is the median redshift of the source distribution, and by definition, $\int dN/dz = 1$. Note that for such a selection function, one can show that its width simply scales with its median value, $\sigma_z \simeq z_m/2$. For convenience we shall take $z_m = 0.33$ as our fiducial model. For all the sky we have set the monopole ($\ell = 0$) and dipole ($\ell = 1$) contribution to zero in order to be consistent with the WMAP data.

¹<http://healpix.jpl.nasa.gov/>

²As a check, we will compare below, in Fig.4.5, the results of the MC1 simulations, which have a fix galaxy map with Gaussian statistics, with the results using the observed SDSS DR5, which is not Gaussian. We find no significant differences, indicating that the level of non-Gaussianity in observations does not influence much the error estimation.

We have run simulations for surveys covering different areas, ranging from an all-sky survey ($f_{sky} = 1$) to a survey that covers only 10% of the sky ($f_{sky} = 0.1$). The latter is realized by intersecting a cone with an opening angle of 37° from the north pole with the sphere. Larger survey areas are obtained by taking larger opening angles. For $f_{sky} = 0.1$ we have done the same analysis taking a compact square in the equator (with galactic coordinates $l = 0^\circ$ to $l = 66^\circ$ and $b = -33^\circ$ to $b = 33^\circ$) and have found similar results. We note that the wide $f_{sky} = 0.1$ survey is comparable in area and depth to the distribution of main sample galaxies in the SDSS DR2-DR3.

3.3.1 Clustering in the simulations

We have computed the angular 2-point correlation function for the galaxy over-density w_{GG} , the temperature w_{TT} and their cross-correlation w_{TG} , as well as their (inverse) Legendre transforms, i.e, the angular power spectra,

$$w(\theta) = \sum_{\ell} \frac{2\ell + 1}{4\pi} C_{\ell} P_{\ell}(\cos\theta) \quad (3.4)$$

$$C_{\ell} = 2\pi \int_{-1}^1 d\cos\theta w(\theta) P_{\ell}(\cos\theta) \quad (3.5)$$

where we denote by P_{ℓ} the Legendre polynomial of order ℓ .

In real space, we define the cross-correlation function as the expectation value of galaxy number density δ_G and temperature Δ_T fluctuations:

$$\delta_G = \frac{N_G}{\langle N_G \rangle} - 1 \quad (3.6)$$

$$\Delta_T = T - T_0 \text{ (in } \mu K) \quad (3.7)$$

at two positions \hat{n}_1 and \hat{n}_2 in the sky:

$$w_{TG}(\theta) \equiv \langle \Delta_T(\hat{n}_1) \delta_G(\hat{n}_2) \rangle, \quad (3.8)$$

where $\theta = |\hat{n}_2 - \hat{n}_1|$, assuming that the distribution is statistically isotropic. To estimate $w_{TG}(\theta)$ from the pixel maps we use:

$$w_{TG}(\theta) = \frac{\sum_{i,j} \Delta_T(\hat{n}_i) \delta_G(\hat{n}_j)}{N_{pairs}}, \quad (3.9)$$

where the sum extends to all pairs i, j separated by $\theta \pm \Delta\theta$. Survey mask and pixel window function effects have been appropriately taken into account using SpICE (Szapudi et al. 2001b,a). This code has been probed to yield correct results not only on simulations but also on real data from surveys with partial sky coverage and complex survey geometries (Fosalba & Szapudi 2004). In Fig.3.1 we show results from the all-sky MC2 simulations, whereas Fig.3.2 displays the same for a survey covering 10% of the sky alone ($f_{sky} = 0.1$). Error bars are computed as the rms dispersion over the MC2 simulations. For the C_{ℓ} 's, we use linear bins with $\Delta\ell = 18$, to get approximately uncorrelated error bars for $f_{sky} = 0.1$ (see Fig.4.2 and chapter 12.4). As shown in the plots, our all-sky simulations are unbiased with respect to the input fiducial model (continuous lines): the mean over 1000 simulations lies on top of the theoretical (input model) curve. For finite area surveys, sample variance makes measurements on the largest scales (i.e, lower ℓ 's) fluctuate around the input theoretical model ³.

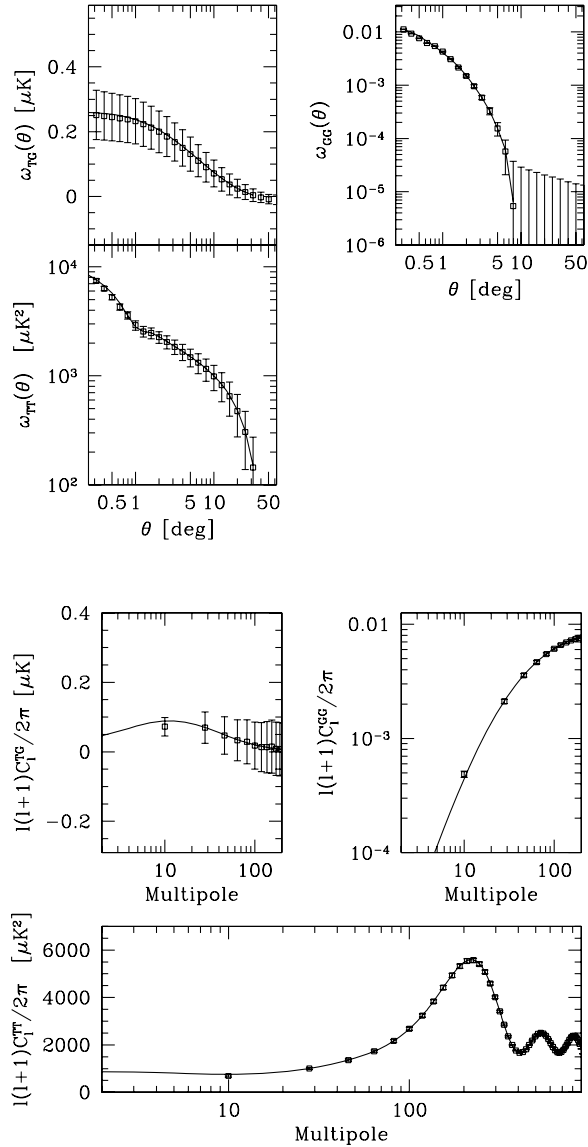


Figure 3.1: 2-point angular correlation function (top panels) and angular power spectra (bottom panels) for all-sky surveys with median depth $z_m = 0.3$. Different panels correspond to TT (Temperature-Temperature), GG (Galaxy-Galaxy) and TG (Temperature-Galaxy) cross-correlation. Errors shown correspond to dispersion over Monte Carlo MC2-type simulations binned with $\Delta_\ell = 18$ (see text for details)

3.3.2 Convergence in simulations

The MC covariance is defined as:

³When we calculate the cross-correlation in a fraction of the sky, there is a residual monopole in the galaxy and temperature maps, which changes the normalization of both fluctuations. In a real survey we are limited by the survey area covered by galaxies and we need to normalize the fluctuations using the local mean, which is in general different from the mean in all sky (because of sampling variance). We find that the cross-correlation calculated with the local normalization with $f_{sky} = 0.1$ is about 10% lower for our fiducial Λ CDM model, but the value can vary for other models and different f_{sky} .

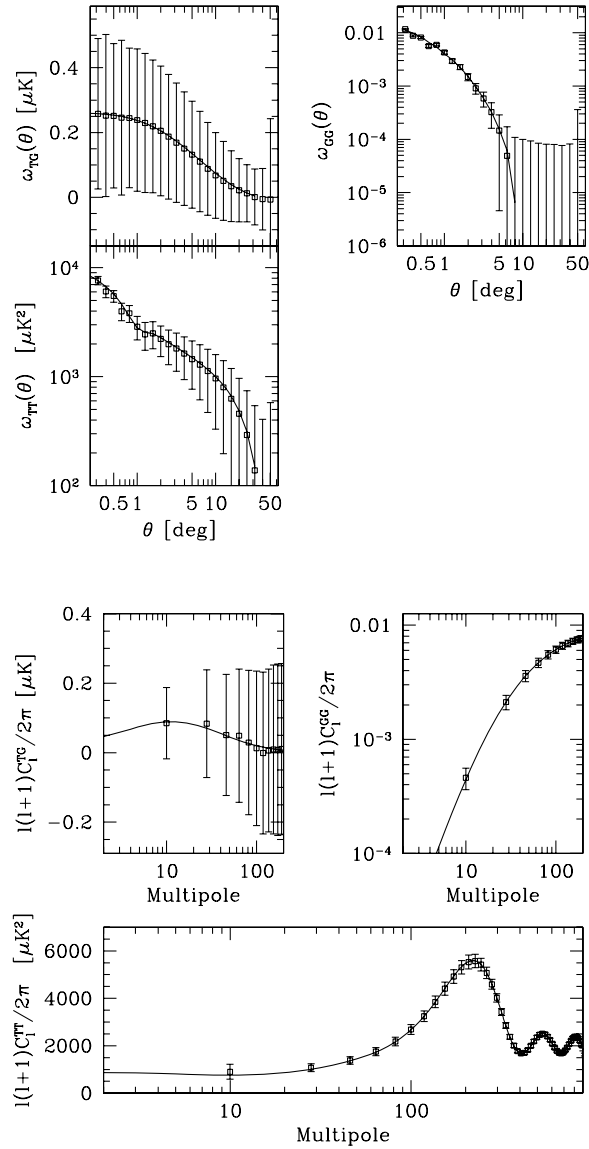


Figure 3.2: Same as Fig.3.1 but for a wide field survey $f_{sky} = 0.1$

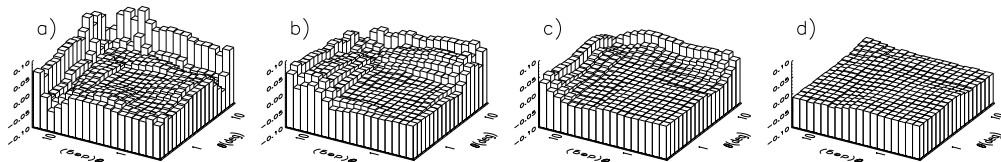


Figure 3.3: Convergence in normalized covariance matrix for Monte Carlo simulations (MC2). We compare covariance when we increase the number of simulations. Here we show the difference between a) the first 100 with respect to the first 200 simulations (100-200), b) 200-400, c) 400-700, d) 700-1000. Results show that one needs at least 700 simulations for the normalized covariance to converge (we use 1000 in our analysis).

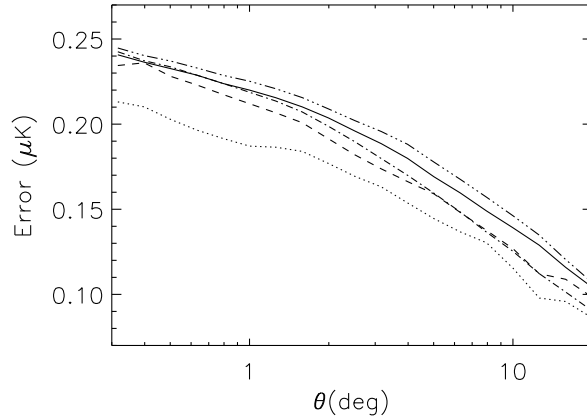


Figure 3.4: Convergence in diagonal error for Monte Carlo simulations. It is shown the error for the first 100 simulations (dotted), 200 (dashed), 400 (dash-dot), 700 (dash-dot-dot) and 999 (solid line). With 200 simulations the accuracy in errors is about 20%.

$$C_{ij} = \frac{1}{M} \sum_{k=1}^M \Delta w_{TG}^k(\theta_i) \Delta w_{TG}^k(\theta_j) \quad (3.10)$$

$$\Delta w_{TG}^k(\theta_i) = w_{TG}^k(\theta_i) - \hat{w}_{TG}(\theta_i) \quad (3.11)$$

where $w_{TG}^k(\theta_i)$ is the measure in the k -th simulation ($k=1, \dots, M$) and $\hat{w}_{TG}(\theta_i)$ is the mean over M realizations. The case $i=j$ gives the diagonal error (i.e, variance).

In order to check the numerical convergence in the computation of the covariance matrix, we compare the results using all 1000 (MC2) simulations with the ones using the first 100, 200, 400 or 700 simulations. For clarity we separate our converge analysis into the diagonal elements (the variance) and normalized covariance, where we divide the covariance by the diagonal elements (see Eq.(4.1)). As shown in Fig.3.3, we find that there is no noticeable difference ($\simeq 5\%$ accuracy) in the normalized covariance from 700 and 1000 simulations. This suggests that 700 simulations are enough for our purposes. To be safe, we shall use all 1000 simulations to derive our main results.

On the other hand, Fig.3.4 shows the convergence on the variance estimation (diagonal elements of the covariance matrix) for an increasing number of simulations. One needs about 200 simulations to converge within 20% accuracy. This is similar to the dispersion in the errors for a given realization due to sampling variance, see Fig.4.7 below. We will use 1000 simulations which will give us better than 5% accuracy in the error estimation from these simulations.

3.3.3 Simulations with a fixed galaxy map (MC1)

We can also calculate Monte Carlo errors by cross-correlating 1000 simulations of CMB with a fixed sky for galaxies (MC1). This is a common practice because it is quite easy to simulate CMB maps and not so easy to simulate galaxy maps. In this case the common (and easiest) thing to do is not to include any cross-correlation signal in the simulated CMB maps. Thus, this approach represents two levels of additional approximations: no variance coming from the galaxy maps and no cross-correlation within the maps. Despite these approximations one expects MC1 errors to be reasonably accurate because most of the variance should come

from the large scale primary CMB anisotropies, and the cross-correlation signal is small in comparison.

Here we want to test in detail what is the accuracy of this approach. We have taken the mean of 20 different cases. Each case has a different fix galaxy map which is paired with 999 CMB maps, which are not correlated. For each fixed galaxy case we obtain a MC1 error, so we can calculate the dispersion of this error with the 20 different galaxy maps. This will be discussed in more detail in §4.6.

3.4 Jackknife errors (JK)

The JK method is closely related to the bootstrap method (Press et al. 1992) which under certain circumstances can provide accurate errors. The idea is that the data is grouped in sub-regions or zones which are more or less independent.⁴ We then use the fair sample hypothesis (ie ergodicity) to estimate the error (variance between zones) for the quantity under study. In the bootstrap methods one defines new sub-samples (which approach statistically independent realizations) by a random selection of sub-regions. In the jackknife method each new sub-sample contains all sub-regions but one. A potential disadvantage of the JK error is that one may think that it can not be used on scales that are comparable to the sub-regions size. This is not necessarily so. Rare events (such as superclusters) can dominate sampling errors on all scales even if they only extend over small regions (Baugh et al. 2004). If JK sub-regions are large enough to encompass these rare events, they can reproduce well errors on all scales. Nevertheless it is clear that a danger with JK errors is that the result could in principle depend on the size and shape of the sub-regions. So this needs to be tested in each situation.

We can therefore calculate the error from each single map using the JK method. To study the JK error in a fraction of the sky of 10%, we divide a compact square area in M zones or sub-regions. Fig.3.5 shows the case $M = 36$, but we have tried different values for $M = 20 - 80$, and find similar results. The JK regions have roughly equal area and shape. This is important; we have found that the JK method could give unrealistic errors when the areas or shapes are not even. To calculate the covariance, we take a JK sub-sample to be all the data removing one of these JK zones, this means that we remove all the pairs that fall completely or partially in the JK zone that is removed. To compensate for the correlation between the JK sub-samples, we multiply the resulting covariance by $M - 1$. The covariance for this case is thus:

$$C_{ij} = \frac{M-1}{M} \sum_{k=1}^M \Delta w_{TG}^k(\theta_i) \Delta w_{TG}^k(\theta_j) \quad (3.12)$$

$$\Delta w_{TG}^k(\theta_i) = w_{TG}^k(\theta_i) - \widehat{w}_{TG}(\theta_i) \quad (3.13)$$

where $w_{TG}^k(\theta_i)$ is the measurement in the k -th sub-sample ($k = 1, \dots, M$) and $\widehat{w}_{TG}(\theta_i)$ is the mean for the M sub-samples. For each of the MC2 pair of simulated maps we have a JK estimation of C_{ij} . We can therefore calculate a JK mean and its dispersion (and distribution) to compare to the true MC2 covariance in the maps.

3.5 Errors in harmonic space (TH)

Theoretical expectations for the errors are the simplest in harmonic space where the covariance matrix is diagonal in the all-sky limit. In particular, for Gaussian fields, one can easily

⁴It is not adequate here to consider individual points or pixels as the units (sub-regions) to bootstrap because they are highly correlated.

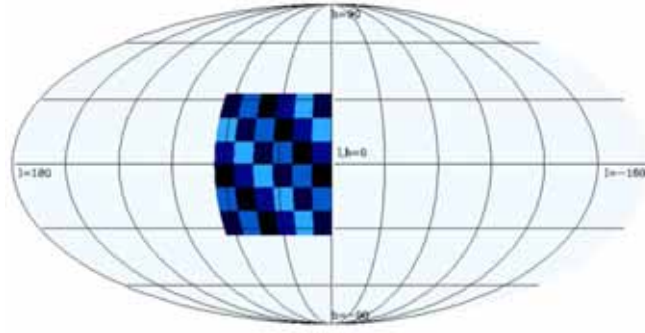


Figure 3.5: Compact square with 36 zones, covering a 10% of the sky, used to calculate JK error in galactic coordinates ($l = 0^\circ$ to $l = 66^\circ$ and $b = -33^\circ$ to $b = 33^\circ$). We see that the shapes and sizes of the zones are similar.

see that the variance (or diagonal error) is,

$$\Delta^2 C_\ell^{TG} = \frac{1}{f_{sky}(2\ell + 1)} [(C_\ell^{TG})^2 + C_\ell^{TT} C_\ell^{GG}]. \quad (3.14)$$

This indicates that the variance of the power spectrum estimator results from quadratic combinations of the auto and cross power, with an amplitude that depends on the number of independent m -modes available to estimate the power at a scale ℓ , which is approximately given by $f_{sky}(2\ell + 1)$. We shall emphasize that this is only approximate and rigorously it is only expected to yield accurate predictions for azimuthal sky cuts. However, as we shall see later, this result is of more general applicability. We note that the dominant contribution to the error and covariance comes from the auto-power of the fields $C_\ell^{TT} C_\ell^{GG}$ involved in the cross-correlation, whereas the cross-correlation signal $(C_\ell^{TG})^2$ only gives a few percent contribution, depending on cosmology and survey selection function.

Partial sky coverage introduces a boundary which results in the coupling (or correlation) of different ℓ modes: the spherical harmonic basis is no longer orthonormal on an incomplete sky. Thus the covariance matrix between different modes,

$$Cov(C_\ell, C_{\ell'}) = \langle (C_\ell - \langle C_\ell \rangle)(C_{\ell'} - \langle C_{\ell'} \rangle) \rangle \quad (3.15)$$

is no longer diagonal (ie see Fig.4.2). Because of the partial sky coverage there is less power on the smaller multipoles. This results in a systematic bias on the low multipoles of C_ℓ that can sometimes be modeled with the appropriate window correction of the survey mask. Here we will use a simple scaling: $C_\ell^{AllSky} / C_\ell^{PartialSky}$ to compensate for this effect.

Using the Legendre transform one can propagate the error ΔC_ℓ in Eq.(3.14) above to configuration space,

$$\Delta^2 w(\theta) = \sum_l \left(\frac{2\ell + 1}{4\pi} \right)^2 P_\ell^2(\mu) \Delta^2 C_\ell, \quad (3.16)$$

where $\mu \equiv \cos\theta$. For the covariance matrix, we find:

$$\begin{aligned} C_{ij} &\equiv Cov(w(\theta_i), w(\theta_j)) \\ &= \sum_l \left(\frac{2\ell + 1}{4\pi} \right)^2 P_\ell(\mu_i) P_\ell(\mu_j) \Delta^2 C_\ell, \end{aligned} \quad (3.17)$$

where $\mu_i \equiv \cos\theta_i$. Eq.(3.17) and Eq.(3.16) assumes that different ℓ multipoles are uncorrelated which is only strictly true for all-sky surveys. We shall see below that this approximation is

quite accurate anyway even for surveys that cover only 10% of the sky, i.e, cosmological parameter contours derived from this expression do not significantly differ from those computed with simulations that take into account the exact covariance matrix.

3.6 Errors in configuration space (TC)

The cross-correlation function in configuration space is estimated by averaging over all pairs of points separated an angle θ in the survey,

$$w_{TG}(\theta) = \langle \Delta T(q) \delta_g(q') \mid_{\hat{q}\hat{q}'=\theta} \rangle_{survey} . \quad (3.18)$$

Marc Manera has derived a formula for the covariance of the estimator in an ensemble of sky realizations. Details of this derivation can be found in Appendix A, in Cabré et al. 2007.

$$C_{ij} = \frac{1}{8\pi^2 P(\theta_i) P(\theta_j)} \int_0^\pi \frac{K[\theta_i, \theta_j, \psi]}{P(\psi)} \sin \psi d\psi \quad (3.19)$$

where the kernel K is given by:

$$K[\theta, \theta', \psi] = \frac{1}{2} [W_{TT}(\theta, \psi) W_{GG}(\theta', \psi) + W_{TT}(\theta', \psi) W_{GG}(\theta, \psi)] + W_{TG}(\theta, \psi) W_{TG}(\theta', \psi) \quad (3.20)$$

and W_X is a mean over the corresponding correlation w_X , with $X = TT, GG$ or TG :

$$W_X(\theta, \psi) = 2 \int_0^\pi d\phi P(\psi, \theta, \phi) w_X(\phi) \quad (3.21)$$

where $\cos \phi = \cos \theta \cos \psi + \sin \theta \sin \psi \cos \varphi$. Survey geometry is encoded in $P(\theta)$ and $P(\psi, \theta, \phi)$ probabilities. These are the probabilities for two points separated by an angle θ or for a triangle of sides ψ, θ, ϕ to fall completely into the survey area if they are thrown randomly on the full sky. For partial sky surveys these probabilities depend mainly on the survey area and can be well approximated by the formula provided in Appendix A (Cabré et al. 2007). Particularly simple analytic expressions can be obtained for a ‘‘polar cap’’ survey (area obtained by intersecting a cone with the sphere) and are given in the Appendix B (Cabré et al. 2007).

This new method of computing errors in real space has several advantages. Since it takes into account the survey geometry, it can provide more accurate errors at large angles where both the jackknife errors and the harmonic-space errors become more inaccurate. Compared to Monte Carlo errors this method is faster because one does not need to generate a large number of sky realizations. What is more, this estimator does not need to rely on any theoretical/fiducial model, because the input can be based on the observed maps, so one can readily apply it to correlation functions measured on the real data to estimate the errors.⁵

⁵A FORTRAN code (named TC-ERROR) which takes as input w_{TG}, w_{TT} , and w_{GG} and compute the covariance matrix and errors for the cross-correlation function, can be obtained upon request from the authors (please contact Marc Manera). Of course, this code can also be used to estimate the auto-correlation error in a single map by just placing $w_{TG} = w_{TT} = 0$.

Chapter 4

Comparison between different error estimators

For each one of the methods presented in the previous section, we next compare the normalized covariance:

$$\hat{C}_{ij} = \frac{C_{ij}}{\sqrt{(C_{ii}C_{jj})}} \quad (4.1)$$

and the diagonal errors (variance) and its associated dispersion.

4.1 Configuration space

As shown in Fig.4.1 all the normalized covariances \hat{C}_{ij} in real space are very similar. The appearance of the plots does not seem to depend strongly on the method we use to estimate them, or the survey area f_{sky} . Here we only show results for 10% and all the sky, but intermediate values yield similar results. However, we want to question if slight differences in the covariance could have a non-negligible impact on cosmological parameter estimation. We will discuss this in detail in §5.3.

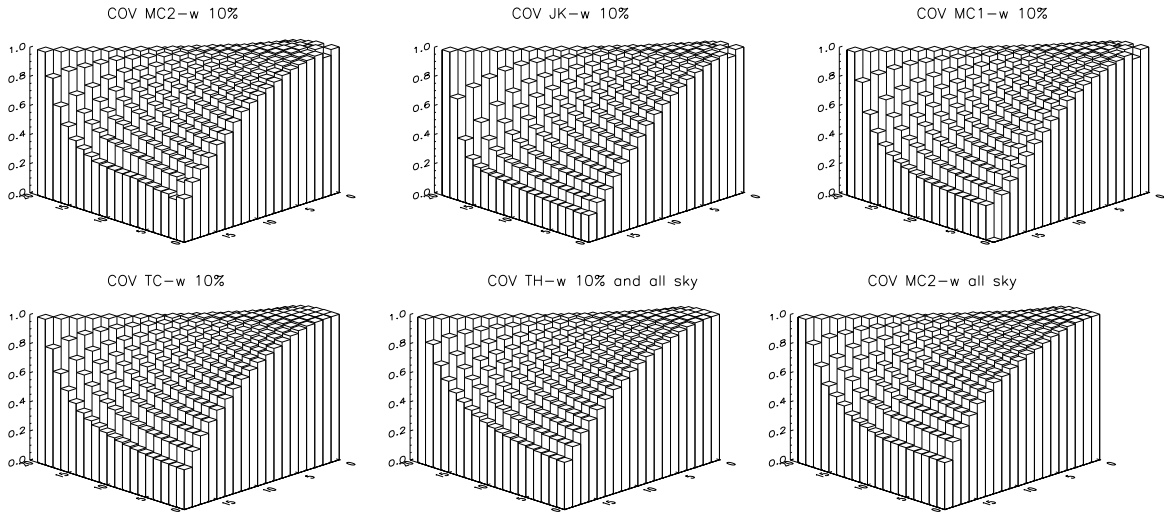


Figure 4.1: Normalized covariances in real space for different methods as labeled in the figure. No significant changes are found for different methods and sky fractions used.

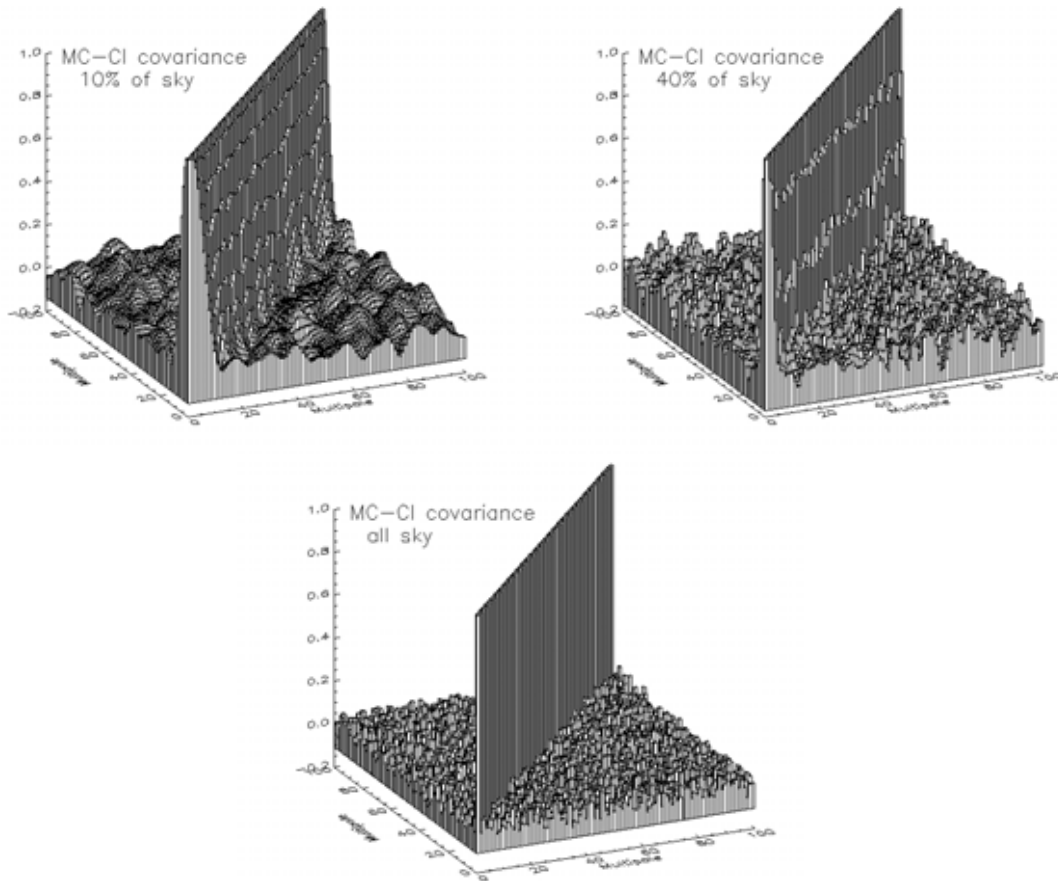


Figure 4.2: Normalized covariances in C_ℓ space from Monte Carlo (MC2) method. The covariance becomes progressively dominated by its diagonal elements as we increase the sky fraction f_{sky} .

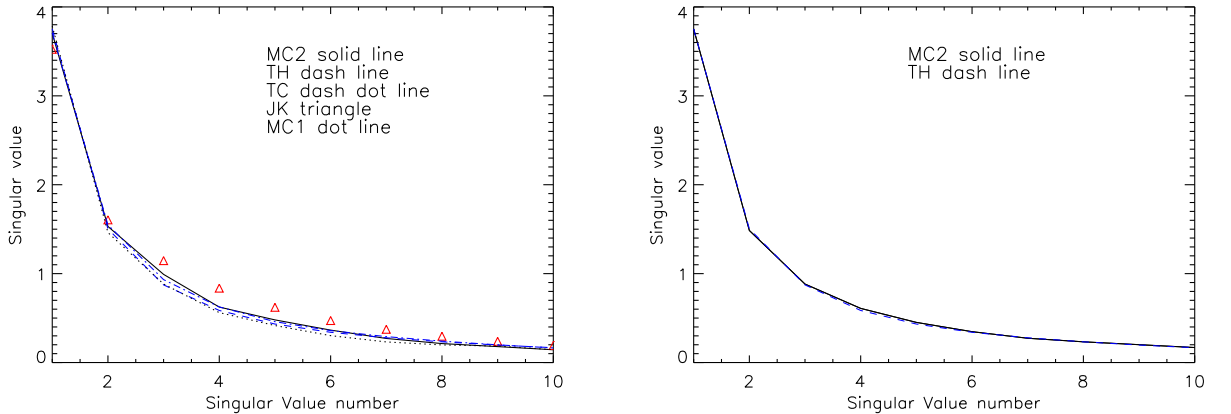


Figure 4.3: Eigenvalues in real space for 10% sky (left panel) and all sky (right).

4.2 Harmonic space

In C_ℓ space, there is no correlation between different l -modes (bins $\Delta\ell = 1$) for the case of all sky (MC2) maps. The normalized covariance matrix is diagonal, as can be seen in the right panel of Fig.4.2. Also shown, in the left and central panels, are the results for 10% and 40% of the sky, where the covariance between modes gives rise to large amplitude off-diagonal elements. This is in sharp contrast to the results in configuration space (in Fig.4.1) where there is no significant difference between normalized covariances in real space when we decrease the area. This is because the main effect of increasing the area in configuration space is the reduction of diagonal errors (which are shown in next section), while in harmonic space there is a transfer of power from diagonal to off-diagonal elements.

4.3 Eigenvalues and Eigenvectors from SVD

To calculate the distribution χ^2 and the signal to noise we need to invert the covariance matrix. We use the Singular Value Decomposition method to decompose the covariance in two orthogonal matrices U and V and a diagonal matrix W which contains the singular values λ_i squared on the diagonal (eg see Press et al. 1992). This method is adequate to separate the signal from the noise:

$$\hat{C}_{ij} = (U_{ik}^T)W_{kl}V_{lj} \quad (4.2)$$

where $W_{ij} = \lambda_i^2 \delta_{ij}$ and \hat{C}_{ij} is the normalized covariance in Eq.(4.1). By doing this decomposition, we can choose the number of modes that we wish to include in the analysis. This SVD is effectively a decomposition in different modes ordered in decreasing amplitude.

We obtain very similar singular values for each mode and for each method, as show in Fig.4.3 for some of the cases (other cases give very similar results).

We can understand the effect of modal decomposition looking at the eigenvectors shown in Fig.4.4, where we have plotted the four dominant eigenvectors as a function of angle: first mode (solid) affects only the amplitude, second mode (dotted) shows a bimodal pattern. The following modes, third (dashed) and fourth (dot-dash), correspond to modulations on smaller angular scales. As can be seen in the figure, we obtain nearly the same eigenvectors in all the cases, in agreement to what was found by direct comparison of the covariance matrices in

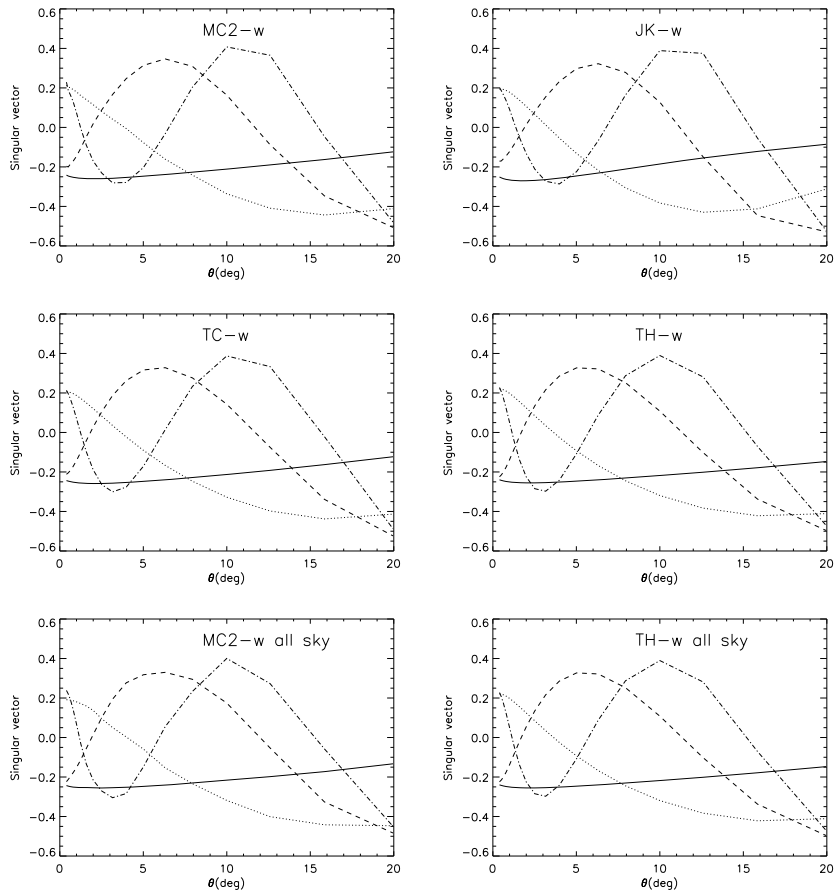


Figure 4.4: Eigenvectors in real space for 10% of the sky and for all sky, as labeled in each panel. First eigenvector is shown as solid lines, second as dotted, third dashed and fourth dot-dash. Results for $MC1-w$ and $TC-w$, not shown here, are very similar.

Fig.4.1. Again, we can ask: are the small differences significant? We will study this in detail in Chapter 5.

4.4 Variance in $w(\theta)$

Fig.4.5 is one of the main results of this chapter. We compare the variance for the different methods, which is the diagonal part of the covariance matrix. By construction, in the limit of infinite number of realizations, the MC2 error from simulations should provide the best approximation to the errors. We have demonstrated (in section §3.3.2) that 1000 simulations are enough for convergence within 5% accuracy. For all sky maps (lower lines in the Figure) we can see that the three methods used: MC2-w, TH-w and TC-w, yield identical results, as expected. For smaller survey areas we do expect some deviations, because of the different approximations on dealing with the survey boundary. For a survey covering 10% of the sky these 3 methods also agree well up to 10 degrees. At larger scales TH-w (dashed lines) starts to deviate, because boundary effects are in fact not taken into account in this method. The JK error (triangles) has a slope as a function of θ that seems less steep than the other methods, but still gives a reasonably good approximation given that the dispersion in the errors is about 20% (as discussed in §4.6 below). Note how on scales larger than 10 degrees the JK method performs better (ie it is closer to MC2) than the TH-w error. The TC method seems

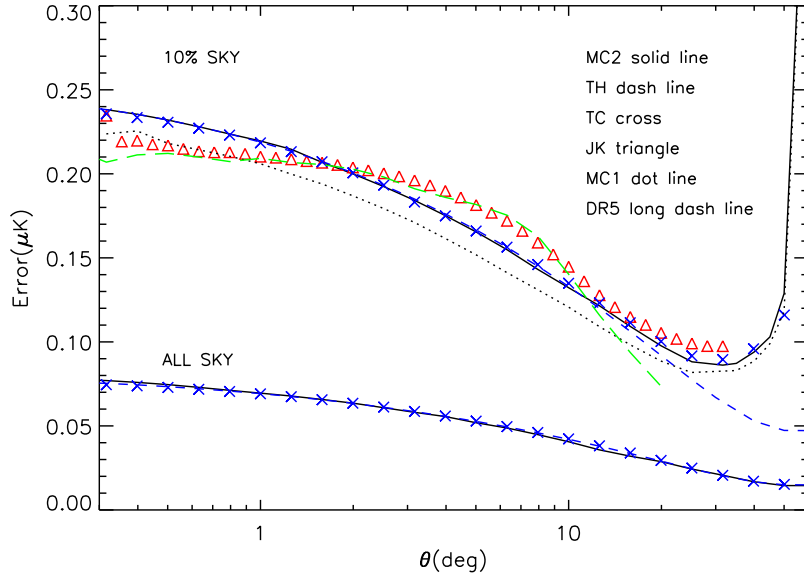


Figure 4.5: Error calculated with different methods (as labeled in the figure) in real space for $\Omega_{DE} = 0.7$. For a map covering 10% of the sky (top lines and symbols), the TC (crosses) and TH (dashed line) theoretical errors work well compared to the Monte Carlo MC2 simulations (solid line), while MC1 simulations (dotted line) seems to underestimate the errors by 10%. The JK method (triangles) seems slightly biased up/down on large/small scales, although all the errors are compatible given the sampling variance dispersion we expect (see Fig.4.7). For all sky maps (bottom lines and symbols), we show how results for MC2 (solid), TH (dashed) and TC-w (cross) agree very well.

to account well for the boundary effects, as it reproduces the MC2 errors all the way to 50 degrees, where all other methods fail.

If we only use one single realization for the galaxies (MC1) the error seems to be systematically underestimated by about 10% on all scales. This bias is expected as we have neglected the variance in the galaxy field and the cross-correlation signal. A particular case of MC1 is done with real data from SDSS DR5 (shown as long dashed line in Fig.4.5). We have used here a compact square of 10% of the sky from the SDSS r magnitude slice of 20-21, which has a redshift selection function similar to the one in our simulations ($z_m = 0.33$). This case works surprisingly well once scaled with linear bias b (estimated by comparing the measured galaxy auto-correlation function with the one in our fiducial Λ CDM model). It happens to closely follow the JK prediction, rather than the MC1 prediction, but we believe this is just a fluke, given the dispersion in the errors (see §4.6) and the uncertainties in the fiducial model.

4.5 Effect of partial sky coverage

We have tested MC2-w, TH-w and TC-w for different partial sky survey areas f_{sky} and obtained similar results. In Fig.4.6 we have plotted the error for a fixed angle of 5 degrees (top) and 20 degrees (bottom) for the different values of f_{sky} . The three methods coincide for large areas. The error scales by a factor $1/\sqrt{f_{sky}}$, as expected.

Notice that errors at angles comparable to the width of the survey are difficult to estimate theoretically because one needs to take into account the survey geometry. Even for a map as wide as 10% of the sky, the survey geometry starts to be important for errors in the cross-correlation above 10 degrees. This is shown in simulations as a sharp inflection that begins at

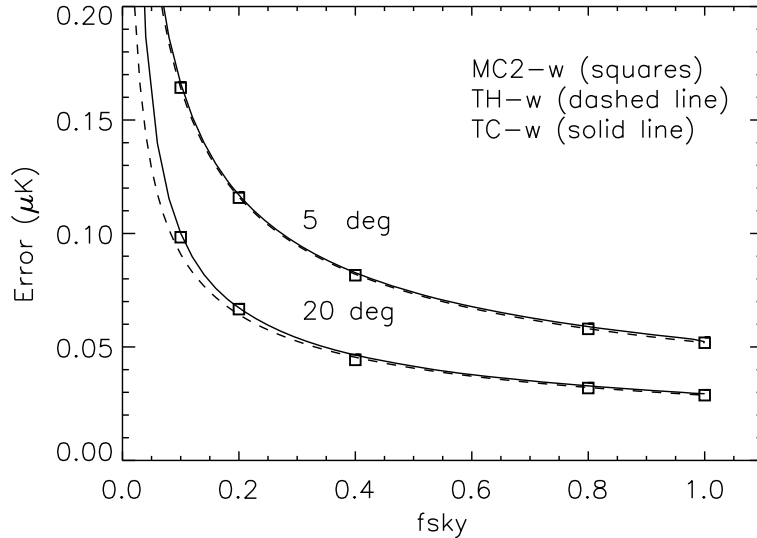


Figure 4.6: Error at a two fix angles: 5 deg (upper lines) and 20 deg (lower lines) as a function of f_{sky} , the fraction of the sky covered by the map. As predicted, errors decrease as $1/\sqrt{f_{sky}}$ in both cases. Note how for small areas, the TC-w prediction (continuous line) performs better than the TH-w model (dashed line) as it better reproduces the MC2 simulations (squares).

30 degrees in Fig.4.5 (solid line) . Our new TC-w method predicts well this inflection, while the more traditional TH method totally misses this feature. This can also be seen in Fig.4.6 for 20 degrees when we approach small values of f_{sky} .

4.6 Uncertainty in $w(\theta)$ errors

To assess the significance of the differences in the error estimation that we find using different methods, we will compute here the sampling uncertainties associated with error estimation. Fig.4.7 shows the sampling dispersion in the error estimates. This can be calculated from the TH and TC approaches by using C_ℓ or $w(\theta)$ measured in each realization as the input model for error theoretical predictions (Eq.(3.16) or Eq.(3.19)), ignoring the covariances. To get an unbiased estimator for unbinned multipoles we apply this window correction: $mean(C_\ell^{allsky})/mean(C_\ell^{10\%sky})$. In Fig.4.7 solid (or dotted) line shows the result of using Eq.(3.16) for each of the MC2 (or MC1) simulations. This produces an error for each realization and we can therefore study the error distribution. The uncertainty in the error (or error in the error) corresponds to the rms dispersion of this distribution. The error propagation Eq.(3.16) is not linear and we find that this produces a bias of 3% when we compare the mean of the propagated errors in each simulation with the propagation of the mean error in all simulations.

We can also calculate the JK-w dispersion of the error, because we have the JK error for each MC2 simulation (remember that we only need one realization to obtain the JK error). The JK-w dispersion (triangles) in Fig.4.7 is quite close to the MC2-w values. They are both of the order of 20% relative to the mean error. This uncertainty can be interpreted as the result of the uncertainties in our input model; typically the model is only known to the accuracy given by the data and a given sky realization will deviate from the 'true' model (i.e, the mean over realizations). Thus, if one chooses to use the estimated values from the data

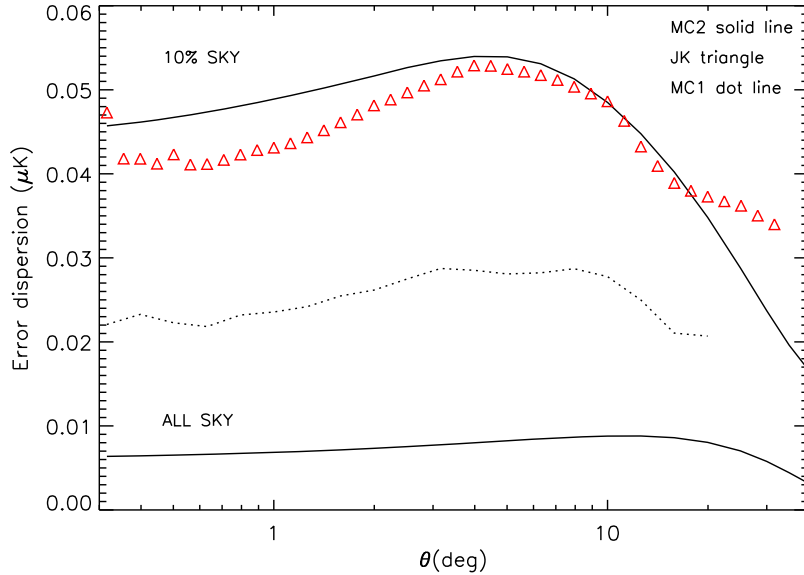


Figure 4.7: Dispersion of the error calculated with different methods in real space for $\Omega_{DE} = 0.7$. For MC2-w (solid line) or MC1-w (dotted lines), we take each pair of MC2 or MC1 simulations as the input for the error in the TH-w calculation in Eq.(3.16). For JK (triangles), we have one error for each MC2 simulation. We can see how the error in the error is of order 20% for MC2 or JK and is lower for MC1 (mainly because one of the maps in each pair is kept fixed). The lower line corresponds to the dispersion in all sky maps.

(or its best fit model) as input to the error estimation, this produces an uncertainty in the error which is of the order of this scatter. This is always the case with the JK errors, which do not use any model, but the uncertainty is similar if we use direct measurements as input to the other error estimations, as shown in Fig.4.7.

For completeness, Fig.4.7 also shows the dispersion for the MC1 error (dotted). There is less dispersion in the MC1 method because one of the maps is always fixed and this reduces both the error and, more strongly, its dispersion.

4.7 Error distribution for JK

Fig.4.8 shows the distribution of JK errors in the MC2 simulations as compared to a Gaussian fit with the same mean and dispersion. Each panel shows the distribution of $w(\theta)$ errors at a given fixed angle. The mean MC2-w error (shown as solid line in Fig.4.5) is shown here by a dotted vertical line, while the mean of the JK errors (shown as triangles in Fig.4.5) corresponds here to the continuous vertical line. We can see here how the MC2-w error and the mean JK-w error are quite similar. The variance in the distribution agrees with the results in §4.6 above. Note also that the JK distribution of $w(\theta)$ errors can be well fitted by a Gaussian. This is important for two reasons. First it shows that there are no important outliers or systematic bias when one uses a JK estimator in a single realization, as is the case with real data. Second, it indicates that the error in the error (ie the rms dispersion of this distribution) entails all relevant information needed to assess in more detail the accuracy of the JK error analysis. One could for example fold the uncertainties in this distribution to assess the significance of a detection.

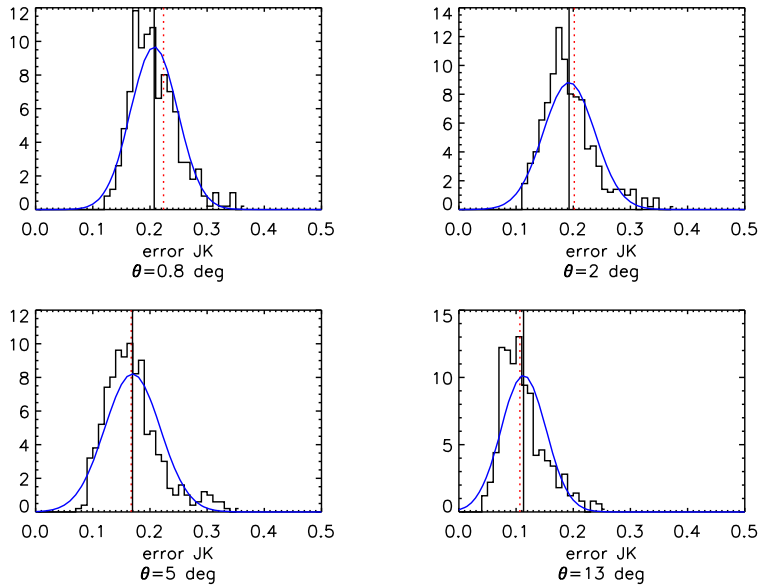


Figure 4.8: Histograms show the error distribution in JK errors from 1000 simulations at different angles. Solid line shows a Gaussian with the same mean and dispersion. Vertical lines correspond to mean JK error (solid) and the true mean MC2 error (dotted).

4.8 Variance in C_ℓ

In C_ℓ space, we have compared MC2 errors to TH theory. Fig.4.9 shows how both errors are hard to distinguish for the case of all sky (middle dashed line matches closely the jagged line). Note the shape of the C_ℓ errors exhibits a broad peak around $\ell = 200$ illustrating the fact that errors are dominated by the C_ℓ^{TT} term. For 10% of the sky the TH error (upper dashed line) obtained theoretically from Eq.(3.14) (with a factor $1/\sqrt{f_{sky}}$ respect to all the sky) is much larger than the MC2 error (upper jagged line) in the simulations. As we have shown in Fig.4.2, there is a strong covariance between different bins when $f_{sky} < 1$, this is in contrast with the TH estimation in Eq.(3.14) which assumes a diagonal covariance matrix. We understand this discrepancy in the variance prediction as a transfer of power from the diagonal to off-diagonal errors.

We can get a better diagonal error estimation by binning C_ℓ in a $\Delta\ell$ that makes the covariance approximately diagonal.¹ When binning by $\Delta\ell$, the theoretical error (TH-C1) in Eq.(3.14) is reduced in quadrature to:

$$\Delta^2 C_\ell^{TG} = \frac{1}{\Delta\ell f_{sky} (2\ell + 1)} [(C_\ell^{TG})^2 + C_\ell^{TT} C_\ell^{GG}], \quad (4.3)$$

This assumes that the bins are independent. Because of the partial sky coverage, the bins are not independent and the above formula will only be valid in the limit of large $\Delta\ell$.

We have tested the above formula for different sky fractions by binning the C_ℓ spectrum in the simulations and estimating the error from the scatter in different realizations. We find that the formula works above some minimum $\Delta\ell$ which roughly agrees with the width of off-diagonal coupling in the covariance matrix estimated from simulations (Fig.4.2). We find

¹This is clear in Fig.4.2 which shows that the covariance is confined to a finite number of $\Delta\ell$ of off-diagonal elements. It is also apparent in Fig.4.9 where the jagged line for 10% of the sky is clearly correlated on scales of $\Delta\ell \simeq 20$, in contrast to the all-sky jagged line which shows no correlation from bin to bin.

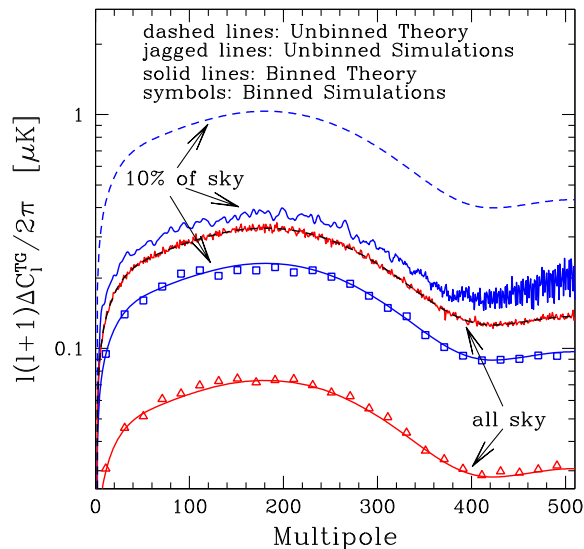


Figure 4.9: Errors in C_ℓ space calculated with (MC2) simulations as compare to (TH- C_ℓ) theory. For all sky maps, the theoretical prediction works well, but for 10% of the sky we see a big discrepancy between theory (dashed lines) and simulations (jagged lines). This is due to covariance between modes and can be solved by binning the C_ℓ spectrum, as shown by the symbols (simulations) and sold line (predictions in Eq.(4.3)).

that $\Delta\ell=20,16,8,1$ for $f_{sky}=0.1,0.2,0.4,0.8$ respectively, diagonalize the covariance matrix and provide a good fit to the above theoretical error for binned spectra. In Fig.4.9 we show the results for $\Delta\ell = 20$ for both all sky (triangles) and 10% of the sky (squares). The theoretical prediction in Eq.(4.3) (solid lines) works very well in both cases, because the covariance with this binning is approximately diagonal.

4.9 Dependence on Ω_{DE}

Fig.4.10 shows a relative comparison of how our error estimation changes for a different cosmology with $\Omega_{DE} = 0.8$ instead of $\Omega_{DE} = 0.7$. The MC error still fits well the TH and TC predictions, but the JK errors seem to underestimate the errors more than in the $\Omega_{DE} = 0.7$ case. This effect is not large given the dispersion in the errors from realization to realization (error bars in Fig.4.10).

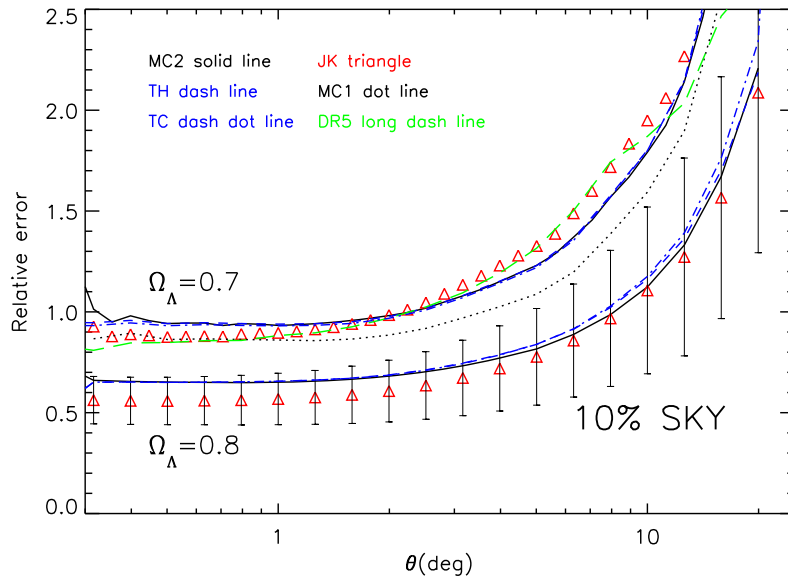


Figure 4.10: Relative error for the two fiducial models $\Omega_{DE} = 0.7$ (top) and $\Omega_{DE} = 0.8$ (bottom). The different methods are labeled in the figure. We see that the relative error depends on the model, and that in the case $\Omega_{DE} = 0.8$ there is also a good agreement within the errors.

Chapter 5

Constraints and significance

ISW measurements can directly constrain dark-energy parameters independent of other cosmological probes. Here we shall use the covariance analysis presented in the previous section to derive significance levels for the cosmological parameter constraints obtained from a cross-correlation analysis.

5.1 Signal-to-noise from $w(\theta)$

The signal-to-noise (S/N hereafter) depends on both the input fiducial model used in the simulations and the covariance matrix method we implement. In this paper we shall invert the covariance matrix using the standard method of singular value decomposition (SVD), see §4.3. In this approach one projects the signal to the eigenvector space of the thus diagonalized matrix and only the most significant eigenvalues are kept for the analysis,

$$\left(\frac{S}{N}\right)_i = \left|\frac{\hat{w}_{TG}(i)}{\lambda_i}\right| = \left|\frac{1}{\lambda_i} \sum_{j=1}^{N_b} U_{ji} \frac{w_{TG}(j)}{\sigma_w(j)}\right|. \quad (5.1)$$

Fig.5.1 shows the S/N for each singular value. All methods agree well even for 10% of the sky. We get excellent agreement for all sky maps.

Because eigenvectors are orthogonal the total S/N is just added in quadrature:

$$\left(\frac{S}{N}\right)_T^2 = \sum_i \left(\frac{S}{N}\right)_i^2 \quad (5.2)$$

Table 5.1 compares total S/N values from simulations and theory for different survey areas. Here by *Simulations* we mean the MC2-w method where we have used 6 singular values and *theory* refers to the different methods, including the TH- C_ℓ approach (see below). We note

S/N	10%	20%	40%	80%	all sky
Simulations MC2-w	1.2	1.7	2.5	3.5	3.8
Theory TH-Cl	1.2	1.7	2.4	3.4	3.8
Theory TH-w	1.2	1.7	2.4	3.4	3.8

Table 5.1: Signal-to-noise as a function of f_{sky} covered in a survey with a broad distribution of sources with median redshift $z_m = 0.33$ for the $\Omega_{DE} = 0.7$ flat Λ CDM model with different error assumptions (see Table 3.1). Similar results are found for TC-w and JK-w methods.

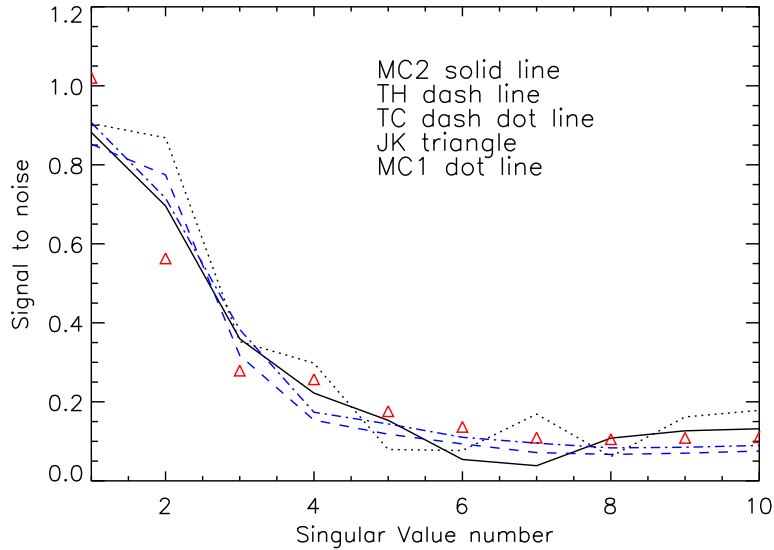


Figure 5.1: Signal-to-noise for 10% of the sky for each singular value. Different lines correspond to methods as labeled.

that we find apparently lower values than quoted in the literature (see e.g, Afshordi 2004). This is due to the low value adopted for Ω_{DE} (i.e $\Omega_{DE} = 0.8$ models yield a S/N ratio ~ 2 larger than our fiducial value $\Omega_{DE} = 0.7$), and the fact that these are predictions for a single broad redshift bin (similar to the selection function for SDSS main sample galaxies), with median redshift $z_m = 0.33$. A combination of several narrow bins at different redshifts will also increase the S/N (see Fig.5.2 and Table 5.2).

5.2 Signal-to-noise forecast from C_ℓ

In harmonic space the S/N is estimated as

$$\left(\frac{S}{N}\right)_T^2 = \sum_\ell \left(\frac{C_\ell^{TG}}{\Delta C_\ell^{TG}}\right)^2 \quad (5.3)$$

using Eq.(3.14) in the denominator. Note in particular that the dominant contribution to ΔC_{TG} in Eq.(3.14), comes from the $C_{TT} C_{GG}$ term and not from C_{TG} which is an order of magnitude smaller. This means that the $(S/N)^2$ approximately scales as:

$$\left(\frac{S}{N}\right)_T^2 \simeq \sum_\ell \frac{C_\ell^{TG} C_\ell^{TG}}{C_\ell^{GG} C_\ell^{TT}} \propto \sigma_8^2 \quad (5.4)$$

and therefore depends strongly on the normalization of the dark matter power spectrum $P(k)$, and is independent of the galaxies bias b . In principle C_{TT} depends on σ_8 but note that σ_8 from CMB is degenerated with several other parameters. We take the approach here of fixing C_{TT} to the observed value and allow σ_8 to vary.

Clearly, the S/N will change depending on the fiducial model used. Fig.5.2 shows this dependence on the plane DE density vs. equation of state, w . Each panel corresponds to different smooth redshift distributions that closely match current or planned surveys (translate to all sky). The upper panels show predictions for SDSS main sample ($z_m = 0.33$), that

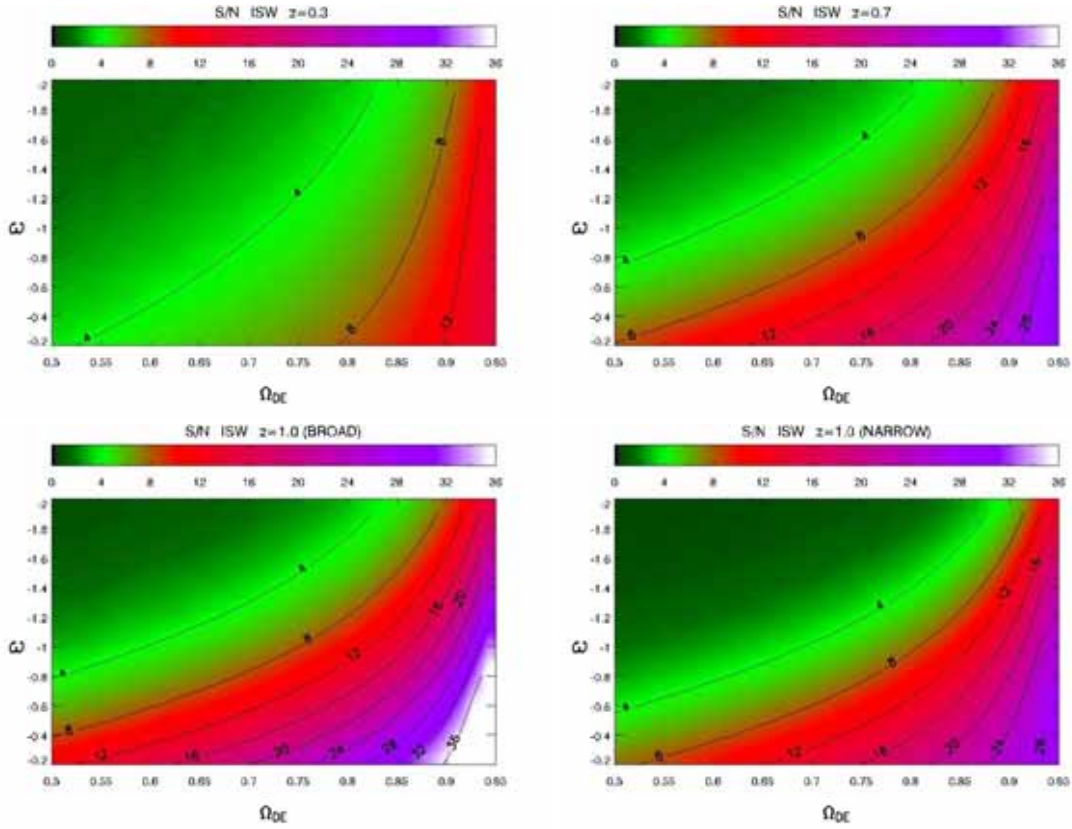


Figure 5.2: All sky values of the S/N for different models. Each panel corresponds to different redshift distribution: SDSS ($z_m = 0.3$), DES ($z_m = 0.7$), DES+VISTA ($z_m = 1$) and DES+VISTA NARROW ($z_m = 1$). Expectations for smaller survey areas are obtained by scaling the displayed values by $\sqrt{f_{sky}}$, where f_{sky} is the sky fraction covered.

S/N	$z_m = 0.33$	$z_m = 0.7$	$z_m = 1$	$z_m = 1$ (N)
$\Omega_{DE} = 0.7$	3.8	6.0	6.3	4.2
$\Omega_{DE} = 0.8$	5.5	9.5	10.6	7.6

Table 5.2: Signal-to-noise for all sky maps in harmonic space for two different values of Ω_{DE} and for galaxy maps with different mean depths z_m . The width of the redshift distribution is given by $\sigma_z \simeq z_m/2$ (see Eq.(3.3)) except in the last case ($z_m = 1$ Narrow), where $\sigma_z \simeq 0.17$

anticipated for the DES ($z_m = 0.7$), and a combined DES+VISTA survey ($z_m = 1$), respectively. For these 3 surveys we use broad distributions as given by Eq.(3.3), with a width that grows linearly with depth, $\sigma_z \simeq z_m/2$. For this rather generic parametrization of the selection function, the S/N monotonically increases with z_m as shown by the 3 upper panels in Fig.5.2, although the differential contribution, $d(S/N)/dz$, drops for sources at $z \gtrsim 0.4$ (see Afshordi 2004 for an analytic account of this effect). As said, the estimations are done for all sky surveys, to be able to compare between them. Expectations for smaller survey areas are obtained by scaling the displayed values by $\sqrt{f_{sky}}$, where f_{sky} is the sky fraction covered.

In particular, for our baseline survey, SDSS, and our fiducial Λ CDM model, we estimate $S/N = 3.8$, what is in good agreement with simulations in configuration space (see Table 5.1). As we sample a wider range of the ISW signal in redshift, the S/N raises by $\sim 60\%$ when we increase the survey depth by a factor ~ 2 to match the depth of the DES-like survey.

However, there is little gain in ISW detection significance when combining DES+VISTA, as the S/N only increases by an additional 5% with respect to the DES survey. For comparison, we also show the case of what we shall call DES+VISTA NARROW survey. This survey has a Gaussian distribution of sources around $z_m = 1$, but with a narrow width, similar to that of SDSS above ($\sigma_z = 0.17$). In this case, the high redshift population of sources brings a poor added value to the baseline survey (SDSS) by improving the S/N by only 10%. As shown in Table 5.2 these conclusions vary somewhat for different values of Ω_{DE} .

We point out that in these estimations we have ignored the lensing magnification bias contribution (see Loverde et al. 2007) which could be important for $z > 1$.

5.3 χ^2 estimation

We shall discuss below to what extent the choice of covariance matrix estimation method affects cosmological parameter constraints. This is specially relevant because current ISW detection significance levels are still rather poor (i.e, at the $4\text{-}\sigma$ level at most, see Chapter 6) and the practical implementation of methods might yield noticeably different results.

We shall compare the methods described in Chapter 3, whereas the fiducial model is the one implemented in the simulations. Our significance levels are derived from a χ^2 statistic:

$$\chi^2 = \sum_{i,j=1}^N \Delta_i \hat{C}_{ij}^{-1} \Delta_j \quad (5.5)$$

where:

$$\Delta_i \equiv \frac{(w_{TG}^E(\theta_i) - w_{TG}^M(\theta_i))}{\sigma_{TG}(\theta_i)} \quad (5.6)$$

is the difference between the "estimation" E and the model M . We have run models for Ω_{DE} from 0.5 to 0.9 and for w from -3.0 to -0.2 and we fix the estimation E to be our fiducial model $\Omega_{DE} = 0.7$ and $w = -1$ which was input in the simulation. The size of the resulting confidence level contours depends implicitly on the best-fit model (i.e, the fiducial model) by construction.

In each case, the error used is the one obtained from the simulations (for cases MC2-w, MC1-w, JK-w, MC2- C_ℓ) or from the theoretical estimator (TH-w and TH- C_ℓ) for the given fiducial model. That is, the errors are not varied as we sample parameter space in the χ^2 estimation. This allows a direct comparison on the contours when using different covariance matrix estimators.

Results are shown in Fig.5.3,5.4 and 5.5. In the different figures we compare the real space MC (MC2-w) result (colored contours) with the other methods (contours traced by solid lines). Contours from different methods agree remarkably well: it does not depend neither on which space we compute the errors and covariance (real or harmonic space), nor on the portion of the sky used. We have checked that small contour differences are compatible once we take into account uncertainties in the errors, as shown in Fig.4.7. Moreover using a diagonal approximation for the C_ℓ covariance matrix to infer the covariance in real space (through the Legendre transform in Eq.(3.16)), works for a small portion of the sky surprisingly well. As explained in section §4.8, when we use the theoretical error in C_ℓ space (TH- C_ℓ) for real data, we should use a bin of width of Δl that varies with the portion of the sky.

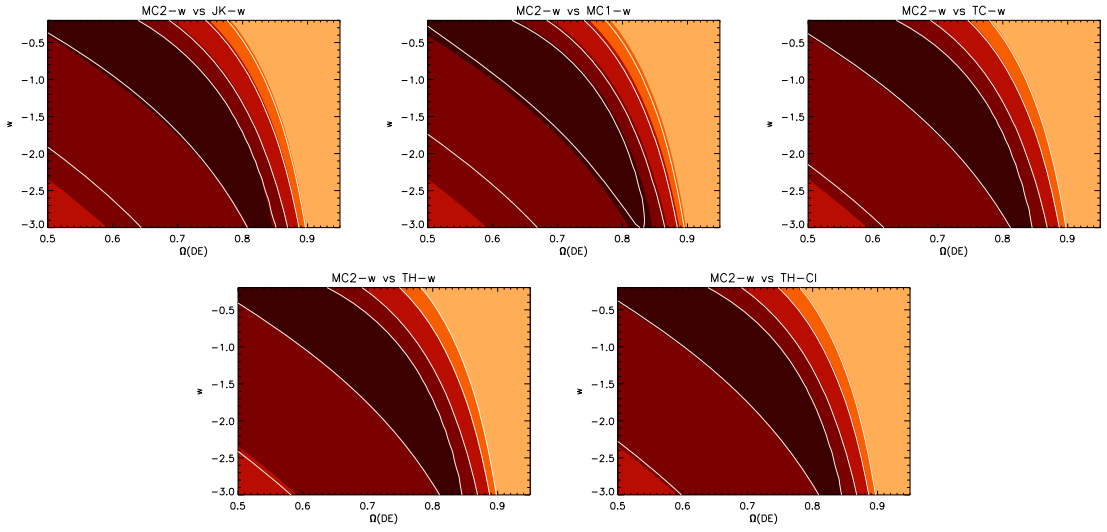


Figure 5.3: χ^2 contours from (MC2-w) simulations (in color) compared to the other methods (solid line): JK-w, MC1-w, TC-w, TH-w, TH- C_ℓ as labeled in each panel. All cases correspond to 10% of the sky. The contour levels are: 0.25, 1., 4. and 9.

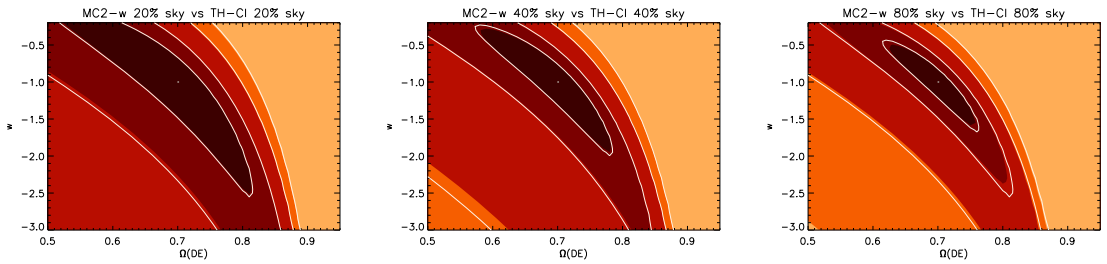


Figure 5.4: Same as Fig.5.3, but here each panel compares to the method TH- C_ℓ for 20%, 40% and 80% of the sky.

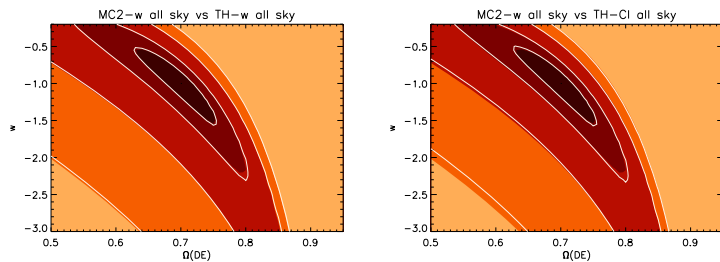


Figure 5.5: Same as Fig.5.3 for all sky maps. Here solid lines correspond to methods TH-w (left panel) and TH-Cl (right panel).

5.4 Best fit model

In this section we investigate how the error method used affects the best fit estimation of cosmological parameters. We fix all the parameters as in the fiducial model, except for Ω_{DE} . We focus on the case of the angular 2-point correlation $w(\theta)$ and compare results for JK-w to those for MC2-w. We do a χ^2 fit of the correlation from each single simulation, which is used as the "E" estimator in Eq.(5.6). This follows what is done with real data where the observations correspond to a single realization. We can make a distribution for all the best

fit values of Ω_{DE} that we obtain from each realization, which is shown in Fig.5.6. The error and covariance used in the fit is in one case the JK-w obtained using this single simulation (dashed line in Fig.5.6) or the MC2-w calculated from all the simulations (continuous line). Despite these differences there is an excellent agreement between the JK-w and the MC2-w results.

We see that the distribution of best fit values is biased towards higher values than the underlying fiducial model value $\Omega_{DE} = 0.7$. In particular, the distribution of best-fit values is skewed, showing a long tail of values smaller than the input model. This is due to the fact that contours in χ^2 (and in the S/N) are not symmetric. The reason for this is the nonlinear mapping between values of Ω_{DE} and the amplitude of $w(\theta)$. When the errors are large, this non-linear mapping transforms an approximate Gaussian distribution (which is a good approximation for the distribution of $w(\theta)$) into a strongly non-Gaussian distribution in Ω_{DE} . When the errors are smaller, as happens for larger Ω_{DE} , the mapping between $w(\theta)$ and Ω_{DE} , is better approximated by a linear relation which results in a more Gaussian distribution. Thus, if we have small enough errors, this bias is negligible, as we can see for the all-sky case shown by the dotted lines in Fig.5.6.

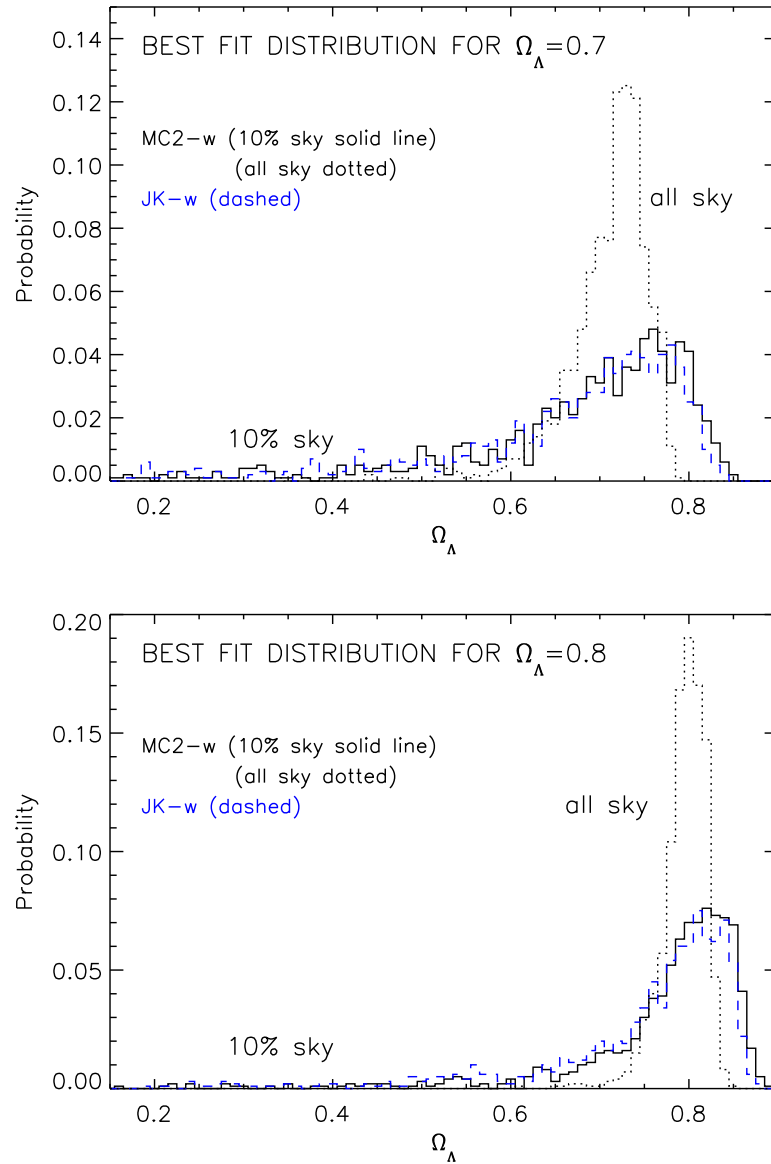


Figure 5.6: Distribution of best fit values for Ω_{DE} fixing $w = -1$ and all the other parameters to the fiducial model. For JK (dotted lines), we use the JK-w error obtained for each simulation. For the MC2 simulations (solid line), we use a fixed error obtained from the dispersion in the simulations.

Chapter 6

Cross-correlation between WMAP 3rd year and SDSS galaxy survey

We cross-correlate the third-year WMAP data with galaxy samples extracted from the SDSS DR4 (SDSS4) covering 13% of the sky, increasing by a factor of 3.7 the volume sampled in previous analysis. The new measurements confirm a positive cross-correlation with higher significance (total signal-to-noise of about 4.7). The correlation as a function of angular scale is well fitted by the integrated Sachs-Wolfe (ISW) effect for LCDM flat FRW models with a cosmological constant. The combined analysis of different samples gives $\Omega_\Lambda = 0.80 - 0.85$ (68% Confidence Level, CL) or $0.77 - 0.86$ (95% CL). We find similar best fit values for Ω_Λ for different galaxy samples with median redshifts of $z \simeq 0.3$ and $z \simeq 0.5$, indicating that the data scale with redshift as predicted by the LCDM cosmology (with equation of state parameter $w = -1$). This agreement is not trivial, but can not yet be used to break the degeneracy constraints in the w versus Ω_Λ plane using only the ISW data. This work can be found in Cabré et al. 2006. Then we compare the results with the cross-correlation with SDSS DR5 noticing that there is no improvement or significant difference in the results.

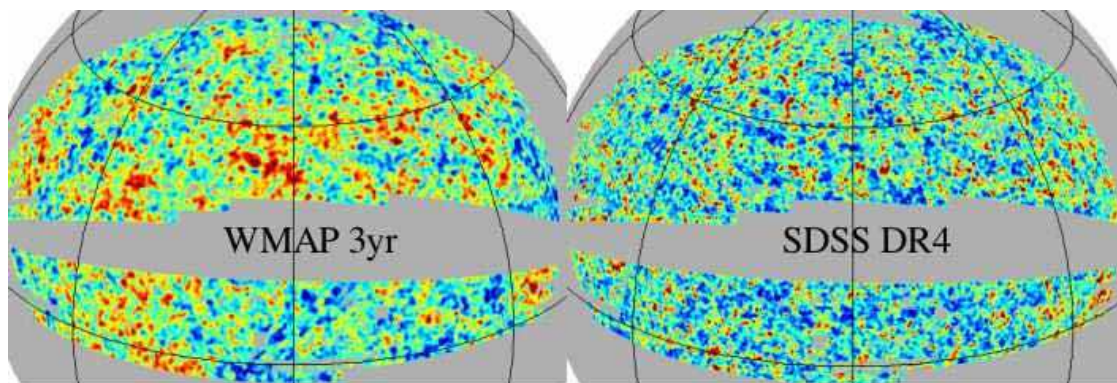


Figure 6.1: SDSS DR4 galaxy density (LRG) fluctuation maps (right panel) compared to WMAP (V-band 3yr) temperature map (left panel). Both maps are smoothed with a Gaussian beam of $\text{FWHM} = 0.3\text{deg}$.

6.1 The Data

In order to trace the changing gravitational potentials we use galaxies selected from the Sloan Digital Sky Survey Data Release 4 Adelman-McCarthy et al. 2006, SDSS4 hereafter,

which covers 6670 deg² (i.e, 16% of the sky). We have also done the same analysis with data from SDSS DR5. We have selected subsamples with different redshift distributions to check the reliability of the detection and to probe the evolution of the ISW effect. All subsamples studied contain large number of galaxies, between 10⁶-10⁷, depending on the subsample. We concentrate our analysis on the North Galactic Cap SDSS4 Area (~ 5500 deg²), because it contains the most contiguous area. We have selected 3 magnitude subsamples with $r = 18 - 19$, $r = 19 - 20$ and $r = 20 - 21$ and a high redshift Luminous Red Galaxy (LRG; e.g. Eisenstein et al. 2001) color selected subsample ($17 < r < 21$, $(r - i) > (g - r)/4 + 0.36$, $(g - r) > 0.72 * (r - i) + 1.7$). Because of the smaller volume, the $r = 18 - 19$ and $r = 19 - 20$ subsamples provide low signal-to-noise ($S/N < 2$) in the cross-correlation with WMAP, and we therefore center our analysis on the two deeper subsamples. The mask used for these data avoids pixels with observed holes, trails, bleeding, bright stars or seeing greater than 1.8.

To model the redshift distribution of our samples we take a generic form of the type:

$$N(z) \sim \phi_G(z) \sim (z - z_c)^2 \exp\left(-\frac{z - z_c}{z_0 - z_c}\right)^{3/2}, \quad (6.1)$$

for $z > z_c$ and zero otherwise. The $N(z)$ distribution of the $r = 20 - 21$ subsample is quite broad with $z_c \simeq 0$ and $z_0 \simeq 0.2$ which results in a median redshift, $\bar{z} = 1.4z_0 \simeq 0.3$ (e.g., Dodelson et al. 2001, Brown et al. 2003). On the other hand, the LRG subsample has a narrower redshift distribution. The first color cut is perpendicular to the galaxy evolutionary tracks in the (g-r) .vs.(r-i) color space and ensures that very few $z < 0.40$ galaxies are selected, which translates into a cut $z_c \simeq 0.37$ in the above $N(z)$ model. The second colour cut is parallel to evolution and perpendicular to spectral type differences and selects only red galaxies with old stellar populations. The faint magnitude limit ($r < 21$) cuts high redshift galaxies ($z_0 \simeq 0.45$), which results in an overall median redshift of $\bar{z} \simeq 0.5$.

We use the full-sky CMB maps from the third-year WMAP data Hinshaw et al. 2007; Spergel et al. 2007 (WMAP3 from now on). In particular, we have chosen the V-band (~ 61 GHz) for our analysis since it has a lower pixel noise than the highest frequency W-band (~ 94 GHz), while it has sufficient high spatial resolution ($21'$) to map the typical Abell cluster radius at the mean SDSS depth. We use a combined SDSS+WMAP mask that includes the Kp0 mask, which cuts 21.4% of WMAP sky pixels Bennett et al. 2003, to make sure Galactic emission does not affect our analysis. WMAP and SDSS data are digitized into $7'$ pixels using the HEALPix tessellation¹. Figure 6.1 shows how the WMAP3 and SDSS4 pixel maps look like when density and temperature fluctuations are smoothed on 0.3 deg scale.

6.2 Cross-Correlation and errors

We define the cross-correlation function as the expectation value of density fluctuations $\delta_G = N_G / \langle N_G \rangle - 1$ and temperature anisotropies $\Delta_T = T - T_0$ (in μK) at two positions \hat{n}_1 and \hat{n}_2 in the sky: $w_{TG}(\theta) \equiv \langle \Delta_T(\hat{n}_1) \delta_G(\hat{n}_2) \rangle$, where $\theta = |\hat{n}_2 - \hat{n}_1|$, assuming that the distribution is statistically isotropic. To estimate $w_{TG}(\theta)$ from the pixel maps we use:

$$w_{TG}(\theta) = \frac{\sum_{i,j} \Delta_T(\hat{n}_i) \delta_G(\hat{n}_j) w_i w_j}{\sum_{i,j} w_i w_j}, \quad (6.2)$$

where the sum extends to all pairs i, j separated by $\theta \pm \Delta\theta$. The weights w_i can be used to minimize the variance when the pixel noise is not uniform, however this introduces larger

¹Some of the results in this thesis have been derived using HEALPix Górski & et al. 1999, <http://www.eso.org/science/healpix>

cosmic variance. Here we follow the WMAP team and use uniform weights (i.e. $w_i = 1$). The resulting correlation is displayed in Fig.6.2. On scales up to 10 degrees we find significant correlation above the estimated error-bars. The dotted and continuous lines correspond to WMAP1 and WMAP3 data respectively, and show little difference within the errors. This indicates that the cross-correlation is signal dominated.

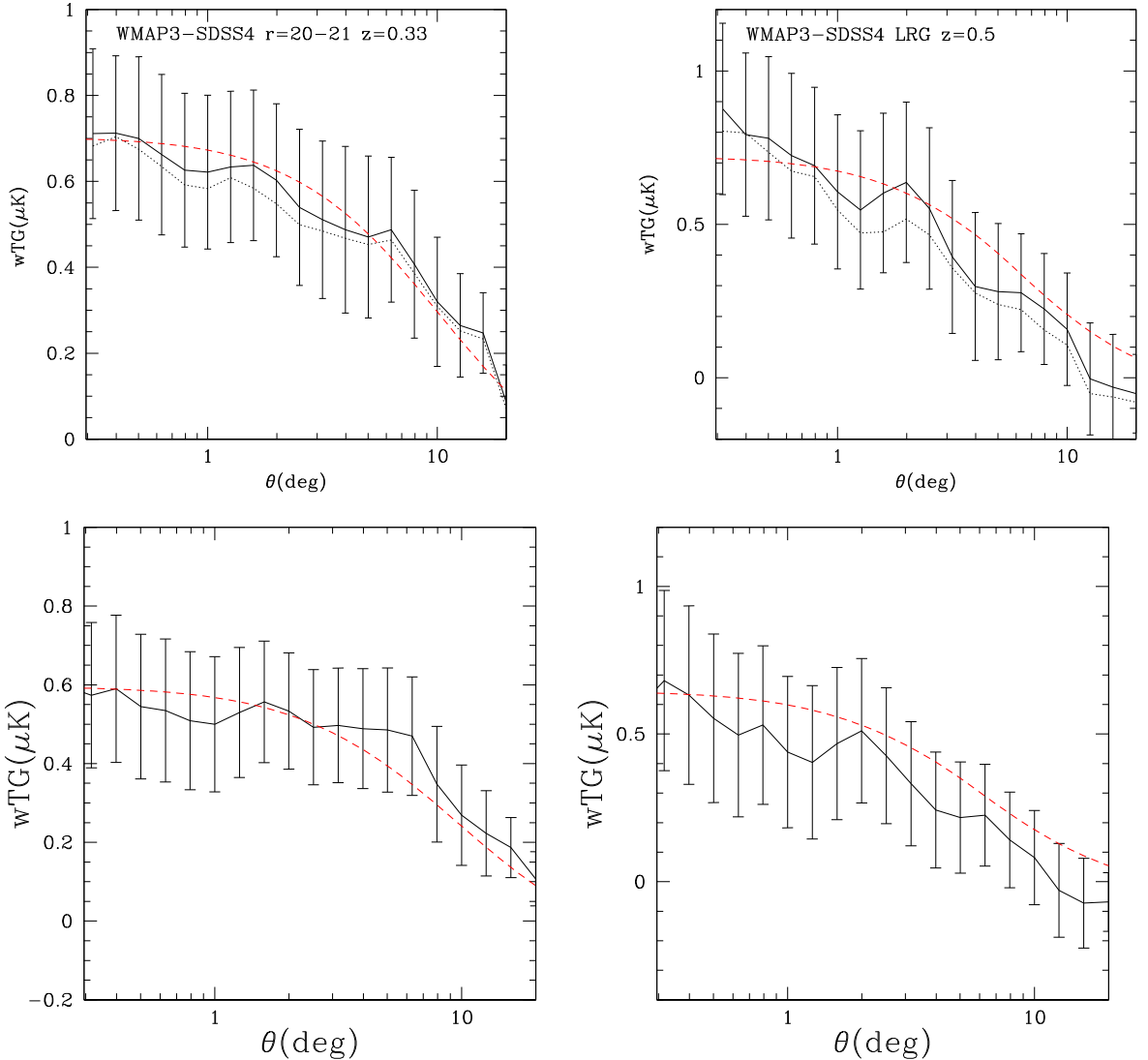


Figure 6.2: The continuous line with error-bars shows the WMAP3-SDSS angular cross-correlation as a function of scale for the $r = 20 - 21$ sample (left) and the LRG sample (right). In the top it is plotted the cross-correlation with SDSS4 and in the bottom with SDSS5. The dotted line corresponds to using the 1st yr WMAP (WMAP1-SDSS4) data, which is very close to the WMAP3 results (continuous line). The dashed lines show the Λ CDM model with $\Omega_\Lambda = 0.83$ for SDSS4 and $\Omega_\Lambda = 0.81$ for SDSS5 (best overall fit) scaled to the appropriate bias and projected to each sample redshift.

We have used different prescriptions to estimate the covariance matrix: a) jack-knife, b) 1000 Monte Carlo simulations c) theoretical estimation (including cross-correlation signal) both in configuration and harmonic space. Our Monte Carlo simulations in b) include independent simulations of both the CMB and galaxy maps, with the adequate cross-correlation signal. All three estimates give very similar results for covariance and the χ^2 results.

$\theta(deg)$	$wTG(20 - 21)$	$wTG(LRG)$
0.316	0.711 ± 0.198	0.876 ± 0.279
0.398	0.712 ± 0.180	0.793 ± 0.266
0.501	0.700 ± 0.190	0.781 ± 0.266
0.631	0.662 ± 0.187	0.724 ± 0.268
0.794	0.626 ± 0.179	0.691 ± 0.255
1.000	0.622 ± 0.179	0.606 ± 0.251
1.259	0.634 ± 0.176	0.547 ± 0.258
1.585	0.637 ± 0.175	0.602 ± 0.260
1.995	0.603 ± 0.178	0.637 ± 0.261
2.512	0.540 ± 0.182	0.552 ± 0.263
3.162	0.511 ± 0.183	0.394 ± 0.249
3.981	0.488 ± 0.194	0.298 ± 0.241
5.012	0.470 ± 0.188	0.281 ± 0.222
6.310	0.488 ± 0.168	0.277 ± 0.192
7.943	0.407 ± 0.172	0.224 ± 0.181
10.000	0.320 ± 0.150	0.158 ± 0.183
12.589	0.265 ± 0.121	-0.004 ± 0.182
15.849	0.247 ± 0.094	-0.031 ± 0.172
19.953	0.086 ± 0.087	-0.052 ± 0.128

Table 6.1: $w_{TG}(\theta)$ for WMAP3-SDSS4.

To compare models we use a χ^2 test:

$$\chi^2 = \sum_{i,j=1}^N \Delta_i C_{ij}^{-1} \Delta_j, \quad (6.3)$$

where $\Delta_i \equiv w_{TG}^E(\theta_i) - w_{TG}^M(\theta_i)$ is the difference between the "estimation" E and the model M . We perform a Singular Value Decomposition (SVD) of the covariance matrix $C_{ij} = (U_{ik})^\dagger D_{kl} V_{lj}$ where $D_{ij} = \lambda_i^2 \delta_{ij}$ is a diagonal matrix with the singular values on the diagonal, and U and V are orthogonal matrices that span the range and nullspace of C_{ij} . We can choose the number of eigenvectors $\hat{w}_{TG}(i)$ (or principal components) we wish to include in our χ^2 by effectively setting the corresponding inverses of the small singular values to zero. In practice, we work only with the subspace of "dominant modes" which have a significant "signal-to-noise" (S/N). The S/N of each eigenmode, labeled by i , is:

$$\left(\frac{S}{N}\right)_i = \left| \frac{\hat{w}_{TG}(i)}{\lambda_i} \right| = \left| \frac{1}{\lambda_i} \sum_{j=1}^{N_b} U_{ji} \frac{w_{TG}(j)}{\sigma_w(j)} \right|. \quad (6.4)$$

As S/N depends strongly on the assumed cosmological model, we use the direct measurements of w_{TG} to estimate this quantity. The total S/N can be obtained by adding the individual modes in quadrature. In our analysis we have used 5 eigenmodes for the $r = 20 - 21$ sample and 3 for the LRG sample. The results are similar if we use less eigenmodes. With more eigenmodes, the inversion becomes unstable because we include eigenvalues which are very close to zero and are dominated by noise.

6.2.1 Comparison with Predictions

We make the assumption that on very large scales the galaxy distribution is a tracer of the underlying matter fluctuations, related through the linear bias factor, $\delta_G(\hat{n}, z) = b(z)\delta_m(\hat{n}, z)$. We estimate $b(z)$ from the angular galaxy-galaxy auto-correlation $w_{GG}(\theta)$ in each sample by fitting to the linear flat Λ CDM model prediction $w_{GG}(\theta)$ and marginalizing over the value of Ω_m . The models have $h = 0.71$, $T_{CMB} = 2.725$, $\Omega_B = 0.022/h^2$, $n_s = 0.938$ and $\Omega_k = 0$. and are normalized to the value of σ_8 that best fits WMAP3 data (Spergel et al. 2007): $\sigma_8 = 0.75 \pm_{0.04}^{0.03}$. With this procedure we find a normalization of $b\sigma_8 \simeq 0.90 - 0.96$ and $b\sigma_8 \simeq 1.02 - 1.12$ for the $r = 20 - 21$ and LRG samples respectively. We marginalize all our results over the uncertainties in both σ_8 and $b\sigma_8$. This also roughly accounts for the uncertainty in the selection function. The predictions of w_{TG} do not change much with the selection function (see §4.1 in Gaztañaga et al. 2006), but the bias estimated from w_{GG} depends strongly on the effective volume covered by $\phi_G(z)$. Because of the marginalization our final results do not change much when we change the median redshift of the sample by $\sim 10\%$, which represents current uncertainties in $N(z)$. But in the case of the LRG it is critical to include not only the correct value of the mean redshift (or z_0 in Eq.(6.1)) but also the redshift cut z_c introduced by the color selection in Eq.(6.1). In previous LRG cross-correlation analysis (eg Fosalba et al. 2003) the value of z_c was neglected. This can over predict $b\sigma_8$, as estimated from w_{GG} , by a factor of two. Uncertainties in the shape of $N(z)$ considered here are within the normalization errors we have already included for σ_8 and $b\sigma_8$. We have also made predictions for the best fit WMAP3 data with $n_s = 1$ which gives different parameters and normalization ($\sigma_8 = 0.79 \pm_{0.06}^{0.05}$) and find very similar results.

Under the above assumptions we are left with only one free parameter, which is Ω_m or $\Omega_\Lambda = 1 - \Omega_m$. Fig.6.3 shows the probability distribution estimated for Ω_Λ from the $\Delta\chi^2 = \chi^2 - \chi_{min}^2$ analysis away from the minimum value χ_{min}^2 . Both samples prefer the same value of Ω_Λ . This is a consistency check for the Λ CDM model. The combined best fit model has $\Omega_\Lambda \simeq 0.83 \pm_{0.03}^{+0.02}$. The predictions for this Ω_Λ best value are shown as a dashed line in Fig.6.2. When doing the same with SDSS DR5 the best fit model shifts to $\Omega_\Lambda \simeq 0.81$, which can be understood within the errors.

Fig.7.1 shows the joint 2D contours for dark energy models with an effective equation of state $w = p/\rho$, assuming not perturbations in DE and a Hubble equation: $H^2/H_0^2 = \Omega(1+z)^3 + \Omega_\Lambda(1+z)^{3(1+w)}$. For each (w, Ω_Λ) we derive $b\sigma_8$ consistently from the galaxy-galaxy auto-correlation data. We also marginalize over the uncertainties in $b\sigma_8$ and over $\sigma_8 \in (0.65, 0.85)$, to account for the WMAP3 σ_8 normalization for $w \neq -1$. The cosmological constant model $w = -1$, however, still remains a very good fit to the data. This is due to the large degeneracy of the equation of state parameter w with Ω_Λ . This degeneracy can be broken by supernovae SNIa data (eg see Corasaniti et al. 2005 and Fig.8 in Gaztañaga et al. 2006).

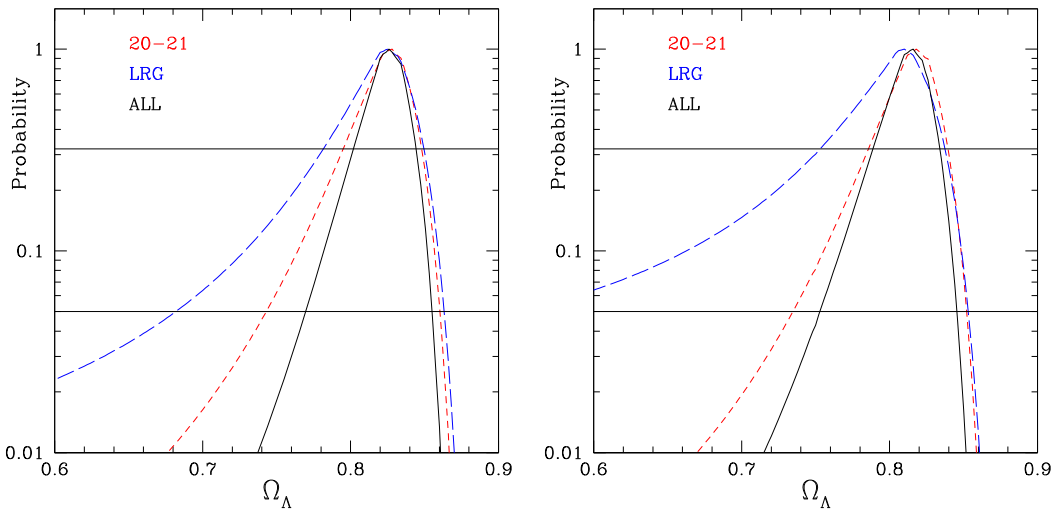


Figure 6.3: Probability distribution: $1 - P_{\chi}[\geq \Delta\chi^2, \nu = 1]$ for Ω_{Λ} in the $r = 20 - 21$ sample (short-dashed line), the LRG sample (long-dashed line) and the combined analysis (continuous middle curve). The range of 68% and 95% confidence regions in Ω_{Λ} are defined by the intersection with the corresponding horizontal lines. The cross-correlation with SDSS DR4 is plot in the left and with DR5 in the right. We don't see any significant difference.

6.3 Systematic errors

In this section, we study systematic effects in the selection of galaxies to explore how they can change our results.

After correcting petrosian magnitudes for extinction we have included some additional cuts to ensure that we work with good galaxies: 1) $\text{petroMagErr} < 0.2$ (error in the apparent petrosian magnitude in filter r) to include only magnitudes that are well measured in r . 2) $0 < g-r < 3$ and $0 < r-i < 2$ to make sure that colors correspond to a galaxy. 3) Surface brightness in r (at half light radius) $\mu_{50} < 24.5$. This cut avoids galaxies which are not well measured. We have plotted the fraction of galaxies after selecting them for each one of the additional cuts, to the number of total galaxies without extra selection, per pixel. For the selection in color (2) and the surface brightness cut (3), the resulting plot is almost completely uniform. This means that these cuts do not include any effect that we can associate with a zone of the sky. Moreover, the clustering does not change significantly, probably because the number of excluded galaxies is not significant. But when we plot the fraction in case (1) we can see some marked yellow zones with lower fraction (red is fraction=1, blue fraction=0) (Fig.6.4). This means that galaxies with bad magnitudes are concentrated in concrete zones.

All this analysis only affects the dimmest galaxies, our slice $m=20-21$. LRG galaxies are not affected for these selection effects. For the case $m=20-21$, we think that we should extract from our analysis all the bad zones traced by the error in magnitude which can bias the analysis. This new mask can be obtained by extracting all the pixels that have a fraction of “good” galaxies lower than 0.65. After removing the bad observational zones, the fraction map becomes almost uniform. A fraction of 0.65 seems enough to remove all the bad zones that can be seen in the figures.

In Fig.6.5 we compare the angular correlation w_{GG} (top panel) and w_{TG} (bottom panel) for different cases. The black line represents our analysis presented in previous section, which excludes bad photometry, suspicious colors or the cut in surface brightness, but it does not exclude bad zones. We think that the adequate result (in red) should exclude the bad zones (fraction < 0.65), while keeping the selection cuts. The green line shows the result when we exclude the bad zones but we do not include any selection in galaxies. Finally the dotted line shows the result when no selection effects or bad zones are taken into account. The green and dotted line are very similar because they are tracing basically the same, no selection in galaxies. This indicates that the area covered by bad zones is not large enough to change the correlation (ie by cosmic variance). But we remark that both these results include galaxies that have an unusually large magnitude error and may not belong to the slice in apparent magnitude $m=20-21$. This could result in slightly deeper sample, which results in a larger depth and a lower amplitude of clustering (which decreases with depth just because of projection effects).

As we can see in Fig.6.5, the amplitudes of w_{GG} and w_{TG} change as it was due some bias in the amplitude of galaxy fluctuations. The relative change in w_{TG} is roughly the squared root of the relative change in w_{GG} . We can use the relative bias in w_{GG} to explain the difference in cross-correlation w_{TG} (ie between the red line and the black line on the bottom panel). This prediction is shown as dotted red. When we eliminate the galaxies with errors above 0.2, we are dropping out statistically the dimmest galaxies and this translates into shallower survey, resulting in a larger amplitude of both w_{TG} and w_{GG} . This effect scales as the selection function $\phi(z)$ for w_{TG} and as its square, $\phi(z)^2$, for w_{GG} , which agrees with the

scaling that is measured. Thus, we believe that the difference between the black and the red line is primarily due to this projection effect. The lesson learned is that one should be careful when working with galaxies which are close to the limit of a given survey.

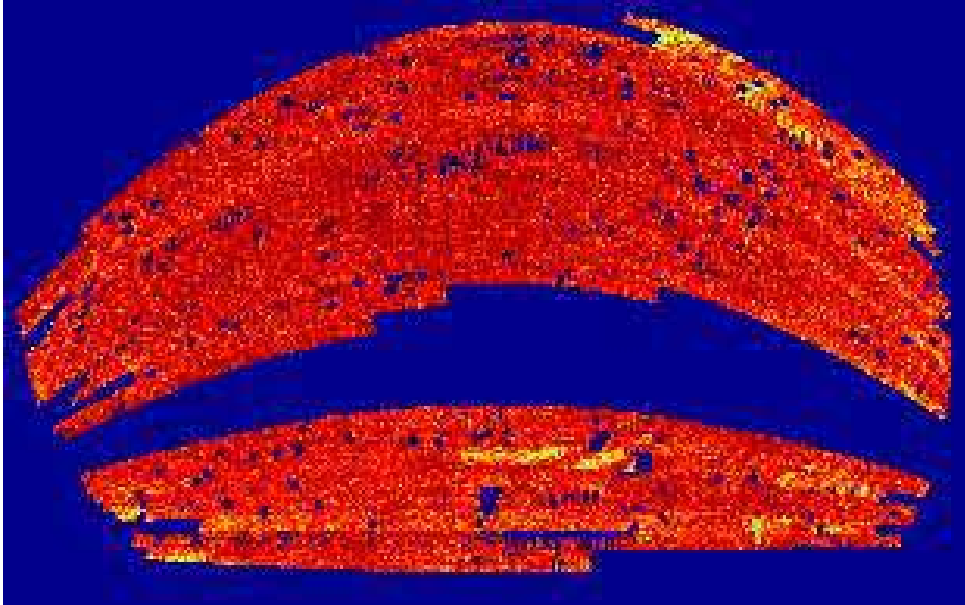


Figure 6.4: We plot the fraction of galaxies with error in the apparent magnitude $r > 0.2$ to the total number of galaxies per pixel (blue=0, red=1)

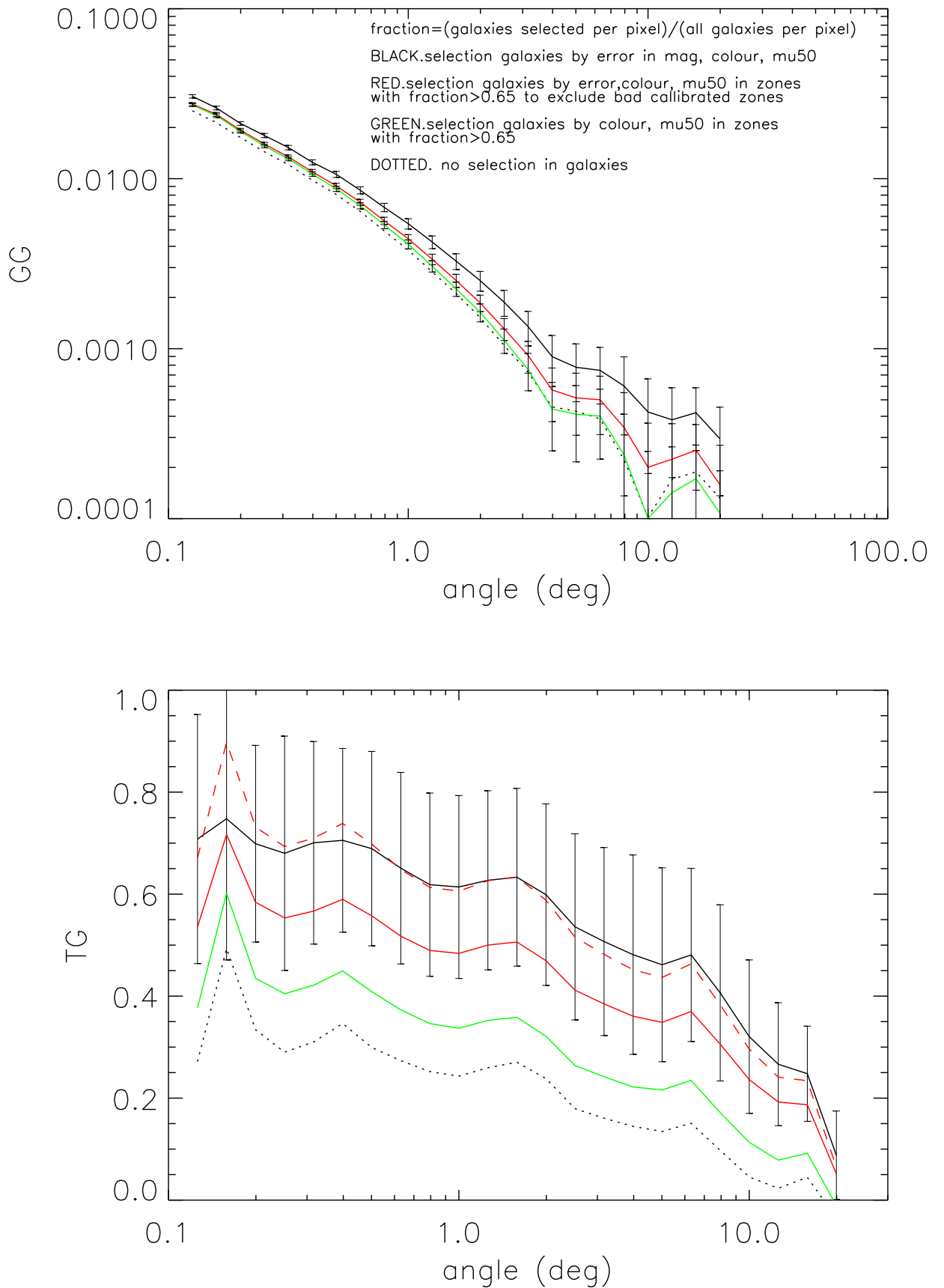


Figure 6.5: Top panel: Galaxy-Galaxy (GG) angular correlation function for different assumptions when selecting the data (as indicated in the figure). Bottom panel: Galaxy-Temperature (TG) angular correlation function with the same colors as top panel, in red dashed we plot the red line multiplied by the linear bias obtained from the top panel GG (between black line and red line)

Chapter 7

Summary & Conclusions for ISW

The objective of our analysis in this part of the thesis was two fold. On one hand we wanted to study in detail different methods for error analysis, in particular the comparison of JK and MC methods. On the other hand, we wanted to check if we could confirm or refute with higher significance the findings of the WMAP1-SDSS1 cross-correlation by Fosalba et al. (2003). With an increase in area of a factor of $\simeq 3.7$ in SDSS4, larger signal-to-noise and better understanding of foregrounds in WMAP3, our new analysis shows that the signal is robust. This is also in line with the first findings using optical (APM) galaxies by Fosalba & Gaztañaga (2004). The cross-correlation signal in WMAP3-SDSS4 seems slightly larger than in previous WMAP1-SDSS1 measurements which results in slightly larger values for Ω_Λ (see Fosalba et al. 2003 and Gaztañaga et al. 2006). This is probably due to sampling variance, as the SDSS4 volume has increase by almost a factor of 4 over SDSS1. We find little difference within the errors in the cross-correlation of WMAP1-SDSS4 and WMAP3-SDSS4 (see Fig.6.2).

The total S/N in Eq.(6.4) of the WMAP3-SDSS4 correlation is $S/N \simeq 3.6$ for the $r = 20 - 21$ sample and $S/N \simeq 3.0$ for the LRG, which gives a combined $S/N \simeq 4.7$, assuming the two samples are independent. We have checked the validity of this assumption by doing a proper join analysis where we include the covariance between the two samples. For the join analysis we find a $S/N \simeq 4.4$ with the first 2 dominant eigenvectors and $S/N \simeq 4.8$ with 4 eigenvectors.

We find that a Λ CDM model with $\Omega_\Lambda \simeq 0.83$ successfully explains the ISW effect for both samples of galaxies without need of any further modeling. The best fit for Ω_Λ for each individual sample are very close. This is significant and can be understood as a consistency test for the Λ CDM model. We also see that there is no significant difference between the results obtained using SDSS DR4 and SDSS DR5.

The equation of state parameter appears to be very degenerate and it is not well constrained by current ISW data alone (see also Corasaniti et al. 2005 and Gaztañaga et al. 2006). Upcoming surveys such as the Dark Energy Survey (DES, www.darkenergysurvey.org), with deeper galaxy samples and more accurate redshift information should be able to break the $w - \Omega_\Lambda$ degeneracy and maybe shed new light on the the nature of dark energy.

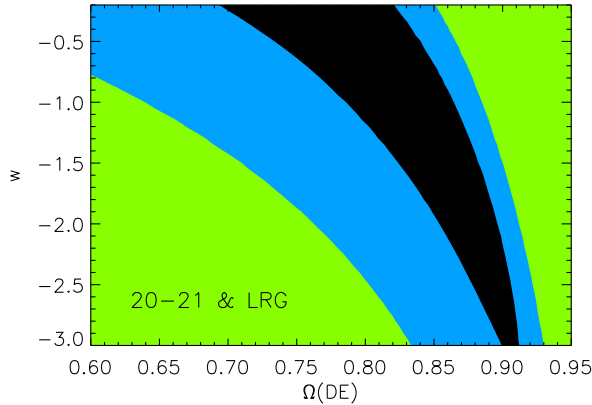


Figure 7.1: Two dimensional contours for Ω_Λ and w , the DE effective equation of state. The inner black contour limits the 1D marginalized 68% confidence region ($\Delta\chi^2 = 1$). The other contour correspond to 95% limits ($\Delta\chi^2 = 4$).

7.1 Conclusions for error estimation

We have run a large number of pairs of sky map simulations, that we call MC2. Each pair is a stochastic realization of an auto and cross correlation signal, that we input to the simulation, what we call the fiducial model. We have focused our attention in testing the galaxy-temperature cross-correlation, so each pair of simulations corresponds to a CMB and a galaxy map. For the fiducial model we take the current concordance Λ CDM scenario. We have run simulations for different values of Ω_{DE} and have tested maps with different fractions of the sky. We have concentrated on the case $\Omega_{DE} = 0.7$ and $f_{sky} = 0.1$ which broadly matches current observations and results in large errors ($> 50\%$).

We are interested in error analysis/forecast and significance estimation. We calculate the correlation between maps and use the different realizations to work out the statistics. We then compare the results to the different approximations that have been used so far in the literature. One of the approximations, that we call MC1, uses Monte Carlo simulations for the CMB maps with a fixed (observed) galaxy map (ie with no cross-correlation signal or sampling variance in the galaxies). We test a popular harmonic space prediction, that we shall call TH (Theory in Harmonic space). We also test jackknife (JK) errors which uses sub-regions of the actual data to calculate the dispersion in our estimator. Finally, we introduce a novel error estimator in real space, that call TC (Theory in Configuration space). For both models and simulations we have assumed that the underlying statistics in the maps is Gaussian. Our main results can be summarized as follows:

- a) The number of simulations needed for numerical convergence (to within $\simeq 5\%$ accuracy) in the computation of the covariance matrix is about 1000 simulations (see §3.3.2).
- b) Diagonal errors in $w(\theta)$ are very accurate in both TH and TC approximations for all sky maps. This is shown in the bottom lines of Fig.4.5. For maps with different fraction of the sky $f_{sky} < 1$, the agreement is also good on small scales ($\theta < 20$ deg) as can be seen in Fig.4.6.
- c) Even for a map as wide as 10% of the sky, the survey geometry starts to be important for errors in the cross-correlation above 10 degrees. This is shown in simulations as a

sharp inflection that begins at 30 degrees in Fig.4.5 (solid line) . Our new TC method predicts well this inflection, while the more traditional TH method totally misses this feature.

- d) If we only use one single realization for the galaxies (MC1) the error seems to be systematically underestimated by about 10% on all scales. This bias is expected as we have neglected the variance in the galaxy field and the cross-correlation signal.
- e) The JK errors do quite well within 10% accuracy on all scales, including the larger scales where boundary effects start to be important (see triangles in Fig.4.5).
- f) The dispersion in the error estimator (error in the error) for individual realizations is of the order 20% (see Fig.4.7). This uncertainty is inherent to the JK method, because one uses the observations (a single realization) to estimate errors. But it is also implicit in other methods because our knowledge of the models is limited by the data and can be thought of as a “sampling variance error”.
- g) S/N (see Fig.5.1) and parameter estimation (see Fig.5.5 and Table 5.1) are equivalent when we do the analysis in configuration and harmonic space. This was expected for all sky maps, but it is not trivial for partial sky coverage (see comments below).
- h) It is possible to propagate errors and covariances from C_ℓ to $w(\theta)$ (harmonic to configuration space) using Eq.(3.16). Starting from a diagonal (all sky) covariance matrix in C_ℓ , the resulting covariance matrix in $w(\theta)$ is quite accurate as compared to direct estimation from simulations.
- i) The above propagation also works well for a map with a fraction f_{sky} of the sky, by just scaling the C_ℓ errors by a factor $1/\sqrt{f_{sky}}$ respect to all the sky. This is surprising because for $f_{sky} < 1$ the covariance matrix in C_ℓ is no longer diagonal (see Fig.4.2) and the actual measured C_ℓ errors in simulations do not simply scale with $1/\sqrt{f_{sky}}$ (see Fig.4.9). Thus, Eq.(3.16) should not be valid. We believe that this works because the two effects compensate. There is a transfer of power from diagonal to off-diagonal elements of the covariance matrix which for the scales of interest (smaller than the survey area) seems to corresponds to a rotation that somehow does not affect the final errors from Eq.(3.16).
- j) If we want to use the popular TH approach in Eq.(3.14) with $f_{sky} < 1$ we need to bin the C_ℓ data in multipole bands of width $\Delta\ell$. The binned spectrum has a diagonal covariance when $\Delta\ell$ is large enough and the error in the binned spectrum approximately follows Eq.(4.3).
- k) When the errors are large (i.e., for partial sky coverage and Λ CDM models with not so large Ω_{DE}) there is a significant bias in the distribution of the recovered best-fit values of Ω_{DE} , as shown in Fig.5.6. This is because of the non linear mapping between Ω_{DE} and the amplitude of $w(\theta)$.
- l) S/N forecasts for future surveys, shown in Fig.5.2 and Table 5.2, strongly depend on the fiducial model used. For example, an all-sky survey with broadly distributed sources around a median redshift $z_m = 1$ and $\Omega_{DE} = 0.8$ can detect the ISW effect with a $S/N \simeq 11$.

What method should be used when confronted with real data? Running realistic simulations seems the best approach, but is very costly because we need of order 1000 simulations

for each model we want to explore. The theoretical modeling of errors seems quite accurate and is much faster to implement. The main advantage of the JK approach is that the errors are obtained from the same data in a model independent way. This is important because real data could surprise our prejudices and also because, in the ISW case, the errors are very large and the data can accommodate different models.

7.2 Conclusions for real data

As an example, consider the analysis presented in Chapter 6 where we cross-correlated the SDSS-DR4 galaxy with the WMAP3 CMB anisotropies. Using the JK approach with $w(\theta)$ they estimate a $S/N \simeq 3.6$ for the $r = 20 - 21$ sample, which has a mean redshift of $z_m \simeq 0.33$. These numbers are high compared with the values in Table 5.2 for $z_m = 0.33$ which for $f_{sky} = 0.13$ gives a low $S/N \simeq 2$, even for $\Omega_{DE} = 0.8$. The dominant contribution to the S/N in Table 5.2 scales as $C_\ell^{TG}/\sqrt{C_\ell^{GG}}$ (ie see Eq.(5.4)) and is therefore independent of bias, but depends on σ_8 . We have noticed that in fact the actual measured values of $C_\ell^{TG}/\sqrt{C_\ell^{GG}}$ in the SDSS DR4-WMAP3 maps are almost a factor of 2 larger than the values in the concordance $\Omega_{DE} = 0.8$ ($\sigma_8 = 0.9$, $n = 1$, $\Omega_\nu = 0$, $\Omega_B = 0.05$, $h = 0.7$) model. This explains the discrepancy in the S/N and illustrates the danger of blindly using theoretical errors that are model dependent. The discrepancy of the concordance model with the SDSS4-WMAP3 measured values of $C_\ell^{TG}/\sqrt{C_\ell^{GG}}$ is not very significant once we account for sampling errors (less than 3-sigma), but it could be an indication of new physics that make the $P(k)$ normalization higher than the concordance model, ie deviations in σ_8 , spectral index n , neutrinos Ω_ν , etc, away from the fiducial model we are considering.

Also note, that there are systematic effects discussed in §6.3 that can bias the amplitude of the cross-correlation measurements. The biases can sometime be as large as the sampling errors which could help reducing the significance of the discrepancies with the LCDM model.

We have also shown that it is possible to use the other theoretical models (ie TC and TH) to make model independent error predictions from observations. Contrary to all other methods, the JK approach does not assume Gaussian statistics, but its accuracy could depend on the model or the way it is implemented (ie shape and number of sub-regions). We conclude that to be safe one needs to validate the JK method with simulations, but there is no reason priori to expect that this method is inaccurate.

In summary, we have presented a detailed testing of different error approximations that have been used in the literature, both in configuration and harmonic space. Contrary to some claims in the literature (see Introduction), we show that the different errors (including the JK method) are equivalent within the sampling uncertainties. By this we mean not only that the error and covariance are similar but also that they produce very similar signal-to-noise (S/N) and recovery of cosmological parameters.